

JULIUS-MAXIMILIANS-UNIVERSITÄT WÜRZBURG
FAKULTÄT FÜR PHYSIK UND ASTRONOMIE
LEHRSTUHL FÜR ASTRONOMIE

BACHELOR THESIS

Long-Term Jet-Kinematics of Blazars in the TANAMI Sample

Author
Wladislaw Schulga

Supervisor
Prof. Dr. Matthias Kadler



ASTRO WÜRZBURG

*A thesis submitted in fulfillment of the requirements
for the degree of Bachelor of Science
in the group of*

Prof. Dr. Matthias Kadler

Chair of Astronomy

Zusammenfassung

Aktive Galaxienkerne (AGNs) sind kompakte Regionen im Zentrum einer Galaxie. Sie sind die leuchtstärksten und beständigsten Quellen elektromagnetischer Strahlung im Universum. Angetrieben werden sie durch Akkretion auf das supermassive schwarze Loch im Zentrum ihrer Wirtgalaxie. In dieser Arbeit ist die Aufmerksamkeit auf AP Librae (AP Lib) gerichtet, welche als ein BL Lac Objekt klassifiziert wird - eine Unterklasse von Blazaren, bei denen die ausgesandten relativistischen Jets direkt auf den Beobachter gerichtet sind. AP Lib hat eine Rotverschiebung von $z = 0.049$. Solche Jets können mithilfe von der Technik von Very Long Baseline Interferometry (VLBI) untersucht werden. Hierbei werden mehrere Teleskope durch sogenannte Basislinien synchronisiert, wodurch man das Auflösungslimit drastisch verbessern kann. Ein konkretes VLBI Programm zur Beobachtung astrophysikalischer Objekte ist TANAMI. TANAMI (Tracking Active Galactic Nuclei with Austral Milliarcsecond Interferometry) ist das größte und am längste laufende VLBI Programm der gesamten südlichen Hemisphäre. Beobachtungen werden mit dem Australian Long Baseline Array (LBA) bei den Frequenzen 2.3 GHz, 8.4 GHz und 22.3 GHz gemacht. Angefangen im Jahr 2010, hat TANAMI nur AGNs beobachtet, die südlicher von -30 Grad Deklination waren. 2020 wurde das Auswahlkriterium für Beobachtungsquellen jedoch auf die gesamte südliche Hemisphäre ausgedehnt. Einer dieser neuen Objekte war der TeV strahlende AP Lib Blazar. AP Lib wurde von 1997 bis 2012 durch das MOJAVE Programm bei 15 GHz mit dem Very Long Baseline Array (VLBA) beobachtet. Unter Verwendung dieser Beobachtungsdaten und einem Jet-Kinematik Modell wurden zwei Modelle erstellt (stationär und bewegt), welche die Jetstruktur im Jahre 2020 - der ersten Beobachtung von AP Lib mit dem TANAMI Programm bei 8.4 GHz - vorhersagen können. Dazu wurden 22 Beobachtungsepochen mit dem Programm DIFMAP mit einem Gaußmodell erstellt. Die resultierenden Komponenten wurden durch alle Epochen hindurch kreuzidentifiziert. Bei diesem Prozess gibt es jedoch keine eindeutige Identifizierung. Dadurch gibt es mehrere Möglichkeiten die Jetstruktur vorherzusagen. Diese erstellten Modelle sollen mit den echten Daten verglichen werden. Abweichungen zwischen der vorhergesagten und der beobachteten Jetstruktur in Jahre 2020 könnten auf beschleunigende oder abbremsende Jet Bewegungen hindeuten, die in Jetmodellen vorhergesagt werden, um die scheinbare Diskrepanz zwischen Doppler Faktoren zu erklären, die aus Radio- und Gammastrahlenbeobachtungen von BL Lac-Objekten abgeleitet werden (die sogenannte Doppler-Krise). Die Ergebnisse dieser Pilotanalyse werden verwendet, um die Perspektiven und Grenzen einer systematischen, groß angelegten Kombination neuer TANAMI-Daten mit VLBA-Archivdaten für die gesamte Stichprobe zu bewerten.

Abstract

Active Galactic Nuclei (AGNs) are compact regions at the center of galaxies which are the most luminous persistent sources of electromagnetic radiation in the universe powered by mass accretion onto the central supermassive black hole of their host galaxy. In this thesis the attention is dedicated toward AP Librae which is classified as a BL Lac object - a subclass of Blazars where they exhibit highly relativistic collimated jets pointed directly towards the observer - and has a redshift of $z = 0.049$. These jets can be investigated by means of the technique of Very Long Baseline Interferometry (VLBI) where one synchronizes multiple radio telescopes via baselines and improves the resolution limit drastically. One concrete monitoring program of such a technique is TANAMI. TANAMI (Tracking Active Galactic Nuclei with Austral Milliarcsecond Interferometry) is the largest and longest-running VLBI monitoring program in the southern hemisphere. Observations are done with the Australian Long Baseline Array (LBA) at 2.3 GHz, 8.4 GHz and 22.3 GHz. Starting in 2010, the TANAMI program originally monitored AGNs exclusively south of -30 degrees declination. Since 2020, the program has been expanded to cover the entire southern sky. One of the newly added sources is the TeV-emitting high-peaked BL Lac object AP Lib. This source was previously observed with the Very Long Baseline Array (VLBA) at 15 GHz from 1997 to 2012 as part of the MOJAVE program. Using a jet-kinematical model derived from these VLBA data, two different models (stationary and moving model) were created to predict the jet structure of AP Lib at the time of the first new TANAMI observation at 8.4 GHz. For this 22 epochs were model-fitted with a Gaussian model. The resulting components were cross-identified. This process however is not unique which means there are multiple possibilities to identify the components through all the epochs. So, as a consequence there are multiple prediction models. These models should be compared with the real observational data. Deviations between predicted and observed 2020 jet structure might be indicative of accelerating or decelerating jet motions, which are predicted in structured-jet models to explain the apparent discrepancy between Doppler factors derived from radio and gamma-ray observations of high-peaked BL Lac objects (the so-called Doppler Crisis). The results of this pilot analysis will be used to assess the prospects and limitations for a systematic larger-scale combination of new TANAMI data with archival VLBA data for the full sample.

Contents

Zusammenfassung	i
Abstract	iii
1 Theoretical background	3
1.1 Active Galactic Nuclei	3
1.1.1 Classification	4
1.1.2 Unification	5
1.2 Radiative processes	6
1.2.1 Synchrotron radiation	6
1.2.2 Synchrotron self-absorption	10
1.2.3 High energy emission	11
1.3 Very Long Baseline Interferometry (VLBI)	11
1.3.1 Radio Interferometry	13
1.3.2 Disturbance effects	16
1.3.3 VLBI monitoring programs	16
1.3.4 Jet kinematics	17
1.3.5 DIFMAP	19
2 Data analysis	21
2.1 Data preparation and modelfitting	21
2.1.1 Kinematic analysis	22
2.2 Simulation	24
3 Results	27
4 Discussion	33
5 Conclusion and Outlook	37
A Appendix	39
Bibliography	57
Danksagung	59

1. Theoretical background

1.1. Active Galactic Nuclei

Active Galactic Nuclei (AGNs) are the most luminous persistent sources of electromagnetic radiation in the universe powered by mass accretion onto the central supermassive black hole of their host galaxy, with typical bolometric luminosities of $10^{43} - 10^{48} \text{ erg s}^{-1}$ (Padovani 1999). This extreme nature leads to a highly astrophysical interest. Especially fundamental questions regarding their composition, formation, collimation and dissipation are still under discussion (Kadler et al. 2015). AGNs are principal probes of the Universe on large scales, so understanding them is essential to studying the formation and evolution of the Universe (Padovani 1999). However, the first discovery of AGNs was made in the early 20th century by Edward Fath (1909), who analyzed a series of 'spiral nebulae' at the Lick Observatory. He wanted to confirm if either these nebulae are unresolved constellation of stars or rather nearby gaseous objects like Orion Nebula by measuring the spectrum of these objects. As a result, most objects showed a continuous spectrum with absorption lines, which is typical for very distant collections of unresolved stars. Nevertheless, some objects also showed very gas-like attributes, namely not only absorption but also emission lines. 1943 Carl K. Seyfert found that a small percentage of galaxies obtain very bright nuclei that are the origin for the broad emission lines which are produced by atoms in a wide range of ionisation states (Carroll & Ostlie 2017). Not until the birth and the further development of radio astronomy over the years Quasars (quasi stellar radio sources) were discovered by Schmidt (1963) - especially the quasar 3C 273. In the optical this object seemed star-like but the redshift analysis ($z = 0.16$) revealed its intergalactic origin. With further observations scientists came to the conclusion that the enormous amount of emitted energy which came from these quasars - concluded from research on luminosity and distance - is produced by mass accretion. At the same time, other objects with active nuclei like Seyfert and radio galaxies as well as Blazars were studied and one found similar results to Quasars - concerning the emission lines. All these results and the rich phenomenology of AGNs lead to many 'flavours' and to a complex 'AGN Zoo'. How all these objects mentioned above and many others were classified and unified will be explained in the next chapters.

1.1.1. Classification

When not otherwise explicitly mentioned this chapter is based on Carroll & Ostlie (2017). One criteria among others to classify AGNs is their radio-loudness which is, according to Kellermann et al. (1989), given by the ratio R_{ro} of the radio flux density S_r and the optical flux density S_o

$$R_{ro} = \frac{S_r}{S_o} \quad (1.1.1)$$

and allows to differentiate the sources into radio-loud ($R_{ro} > 10$) and radio-quiet ($0.1 < R_{ro} < 1$) objects. Another approach is to study the optical spectra of the sources. AGNs with broad emission lines are called type 1 sources while those with narrow emission lines are called type 2 sources. Additionally there is one type with weak or unusual line emission (type 0) (Urry & Padovani 1995).

Seyfert galaxies for example are radio quiet spiral galaxies with a bright core which are divided in two subclasses based on their optical spectra Seyfert I have quite variable X-ray emission which can change on timescales from days to hours. Seyfert II in contrary have weak X-ray emission.

An example for a radio-loud AGNs are the so called **radio galaxies**. Radio galaxies are extremely bright at radio wavelengths and can be divided into two classes according to their emission line properties, similar to Seyfert galaxies. Broad line radio galaxies (BLRG) show broad and narrow emission lines and have bright, starlike nuclei surrounded by very faint, hazy envelopes. Narrow line radio galaxies (NLRG) show only narrow emission lines and their host galaxies are giant or supergiant elliptical galaxies. According to Fanaroff & Riley (1974) radio-loud AGNs can be additionally divided into two luminosity classes based on the ratio R_{FR} of the distance between the brightest spots of radio emission on either side of the center to the full extend of the radio source. Sources with $R_{FR} < 0.5$ were placed in class I (FRI) and sources with $R_{FR} > 0.5$ in class II (FRII). In other words, FRI galaxies radio luminosity diminish with increasing distance from the core and have two jets, whereas FRII galaxies tend to be most radio-bright at the end of the lobes and show only one recognizable radio jet. Another important type of objects are **quasars** (quasi-stellar radio sources). Quasars are very distant (redshifts up to $z > 7$ (Wang et al. 2021)) sources with overwhelming brightness and have a starlike nuclei surrounded by faint fuzzy halos. Sometimes this fuzzy halo can be resolved into a faint parent galaxy. Quasars can also be divided into radio-loud quasars (QSR) and radio-quiet quasars (QSO). Furthermore QSRs can be separated - depending on the value of their radio spectral index α_r - into steep-spectrum radio quasars (SSRQ, $\alpha_r > 0.5$) and flat-spectrum radio quasars (FSRQ, $\alpha_r < 0.5$). Since FSRQs have multifrequency spectra which are dominated by non-thermal emission, they are also included in 'type 0'. The most relevant AGN class for this thesis is the class of **blazars** which is defined by rapid variability and a high degree of linear polarization at visible wavelengths. The most prominent blazar is BL Lacertae located in the

Type	Radio Loudness	Emission Lines	Luminosity	Jets?	Radio Morphology
Seyfert 1	RQ	B+N	Low	-	-
Seyfert 2	RQ	N	Low	-	-
QSO (type 1)	RQ	B+N	High	-	-
QSO (type 2)	RQ	N	High	-	-
BLRG	RL	B+N	Low	Yes	FR1
	RL	B+N	High	Yes	FR2
NLRG	RL	N	Low	Yes	FR1
	RL	N	High	Yes	FR2
BL Lac	RL	-	Low	Yes	Compact
FSRQ	RL	B+N	High	Yes	Compact

Table 1.1.: Simplified classification of AGNs with only a few parameters mentioned above.
RQ = radio-quiet, RL = radio-loud, B = broad emission lines, N = narrow emission lines

constellation of Lacerta (latin for lizard). The irregular variation in its brightness lead originally to the classification as a variable star. The luminosity doubled up in a week and changes by a factor of 15 in timescales of months. Despite its stellar appearance, the spectrum shows only a featureless continuum with very weak absorption and emission lines. Blazars that show similar properties to BL Lacertae are therefore called BL Lac objects. In general, BL Lac objects are also characterized by weak or absent emission lines, beside the above mentioned high polarization and rapid variability. To visualize the astonishing time variability: the luminosities can change by up to 30% in just 24 hours and even by a factor of 100 over a longer period of time. 90% of all BL Lacs are in elliptical galaxies.

To summarize: Although there is a big AGN zoo, it became clear that there are only few parameters which determine the flavour of an AGN. Within the scope of this thesis the parameters are restricted to: radio-loudness, width of the emission lines and the luminosity. It is mentionable that there are attempts to improve the classification model by adding parameters like accretion rates or by using a time dependent systems since all the mentioned parameters change with time (Padovani et al. 2017). The classification of AGNs is also listed in Tab.1.1 taken from Kadler (2023) ¹

1.1.2. Unification

Although there are many different types of AGNs, as shown in Sect. 1.1.1, they can be catalogued and unified with the unification model created by Urry & Padovani (1995). According to them all different kinds of AGNs follow the same physics. The difference in structure of certain objects arise from different viewing angles. Since the main physics

¹Extragalactic jets, Lecture on extragalactic jets held in the summer term

of AGNs is described by few parameters, the general architecture of AGNs could be developed and is presented here in a **Unification Scheme**. There is a supermassive black hole in the center of the system with typical mass of $10^6 M_{\odot}$, where M_{\odot} is one solar mass and a diameter of about 1 AU (Padovani 1999). The only relevant parameters for an astrophysical Black Hole (BH) are its mass and spin, which also are very important parameters to determine the observable features of an AGN. More massive BH are easier to detect, because they are more luminous. This results from the Eddington ratio which is the ratio between the observed luminosity and the Eddington luminosity, $L_{Edd} = 1.31046(M/10^8 M_{\odot}) \text{erg/s}$. This is the maximum isotropic luminosity a body can achieve when there is balance between radiation pressure (on the electrons) and gravitational force (on the protons) (Padovani et al. 2017). The BH is surrounded by an accretion disc which is responsible for the radiation, since potential and kinetic energy are converted in thermal energy. Around the BH and accretion disc, the so called broad line region with a density number of electrons of roughly $n \approx 10^{10} \text{cm}^{-3}$ is located, where broad emission lines are formed. The BH and the accretion disc are obscured by a dust torus with a range from 0.01 to 10 parsec (pc) (Burtscher et al. 2013). Outside the opaque torus is the narrow-line region with a density number of electrons of roughly $n \approx 10^4 \text{cm}^{-3}$, where the narrow emission lines are formed. This also explains the appearance of different types of AGNs in the classification. The main aspect here is to differentiate whether the inner region are visible (Type 1) or not (Type 2). In Type 2 galaxies the inner region obscured by a dust torus, so they have weaker emissions since the radiation is absorbed by the dust torus e.g the beforementioned x-ray emissions of Seyfert I and II. In radio-loud AGNs, the BH produce highly collimated jets which emerge in opposite direction from the BH and can extend as far as 0.1 to several times 100 kpc (Padovani 1999). So different viewing angles between the line of sight and the jet axis result in different classes of an AGNs 1.1.

1.2. Radiative processes

To understand the emission and absorption processes which one observes in a large variety in AGNs it is essential to understand the interaction between photons and particles and particles with each other. The highest photon energies are reached through inverse Compton processes in the jet or in a plasma close to the accretion disk whereas the emission processes in the jet are dominated by synchrotron emissions. In this section all these phenomena will be discussed based on Rybicki & Lightman (1979).

1.2.1. Synchrotron radiation

Accelerated charged particles radiate. For non relativistic velocities the Larmor's formula for emission power from a single accelerated charge q is given by :

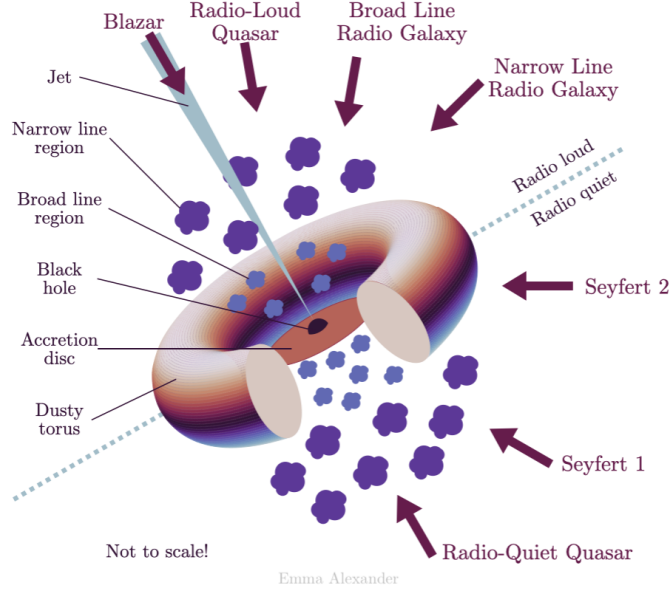


Figure 1.1.: All important classes of AGN are unified in one picture according to Padovani (1999) adopted by emmaalexander . The observed objects are respresented through the red arrows which also shows the viewing angle. The picture is also separated in radio-loud (upper part) and radio-quit (lower part) AGNs.

$$P = \frac{2q^2\vec{a}^2}{3c^3} \quad (1.2.1)$$

with \vec{a} as acceleration and c as light speed.

For a particle which is moving with relativistic speeds Larmor's formula reads:

$$P = \frac{2q^2}{3c^3}\gamma^4(\vec{a}_\perp^2 + \gamma^2\vec{a}_\parallel^2) \quad (1.2.2)$$

in which \vec{a}_\perp is the perpendicular and \vec{a}_\parallel is the parallel component of the acceleration.

The relativistic equations of motions for a certain particle of mass m and charge q in a magnetic field \vec{B} are given by:

$$\frac{d}{dt}(\gamma m \vec{v}) = \frac{q}{c} \vec{v} \times \vec{B} \quad (1.2.3)$$

$$\frac{d}{dt}(\gamma mc^2) = q \vec{v} \cdot \vec{E} = 0 \quad (1.2.4)$$

in which v is the velocity and \vec{E} the electric field.

From Eq.1.2.4 one can see that $\gamma = \text{const.}$ Writing the velocity as a sum of components (perpendicular and parallel) along the field and in a plane normal to the field $\vec{v} = (\vec{v}_\perp + \vec{v}_\parallel)$

gives:

$$\frac{dv_{\parallel}^{\vec{}}}{dt} = 0 \quad (1.2.5)$$

and

$$\frac{dv_{\perp}^{\vec{}}}{dt} = \frac{q}{\gamma mc} v_{\perp}^{\vec{}} \times \vec{B} \quad (1.2.6)$$

what leads to a differential equation describing a uniform circular motion. If one combine the solutions for this circular motion and the uniform motion along the field (v_{\parallel}) one get a helical motion with a rotation frequency (gyration) of:

$$\omega_B = \frac{qB}{\gamma mc} \quad (1.2.7)$$

which results in:

$$a_{\perp} = \omega_B v_{\perp} \quad (1.2.8)$$

Combining this information with Eq.1.2.2 one obtains the total emitted radiation:

$$P = \frac{4}{3} \sigma_T c \beta^2 \gamma^2 U_b \quad (1.2.9)$$

in which $\sigma_t = 8\pi r_0^2/3$ is the Thomson cross section, $r_0 = q^2/mc^2$ and $U_b = B^2/8\pi$ is the magnetic energy density.

Since we are talking about radiation at relativistic speeds there are two important effects which have to be considered, namely relativistic beaming and the lighthouse effect. Relativistic beaming is the process in which relativistic effects affect the apparent luminosity of emitting matter that is moving at speeds close to the speed of light. So, if, for example, a cloud of gas is moving towards an observer, its emitted radiation would appear brighter than that of a cloud in rest. On the other side, the emission would appear fainter if the cloud moves away from the observer. Because of this effect the emitted radiation fields appear to be concentrated in a narrow cone directed into the particles' velocity direction with a angular width of $1/\gamma$. According to Eq.1.2.3, the acceleration of the particles is perpendicular to their velocity, so the angular distribution of the emission looks like that which is shown in Fig.1.2.

Considering this effect and the fact that the electron moves in a helical motion as mentioned above, an observer registers pulsed radiation of the lenght $\delta t = (\gamma^3 \omega_b \sin(\alpha))^{-1}$ if it crosses his line of sight see Fig.1.3. As one can see, the width of the observed pulses is smaller than the gyration period by the factor of γ^3 . This is the reason why the observed frequency of radiation is much greater than the gyration frequency.

The following considerations are based on (Kembhavi & Narlikar 1999). An isolated particle is indeed not the most realistic scenario in the nature. So, assume an ensemble



Figure 1.2.: Angular distribution of the radiation of a particle whose acceleration is perpendicular to its velocity. Taken from Rybicki & Lightman (1979)

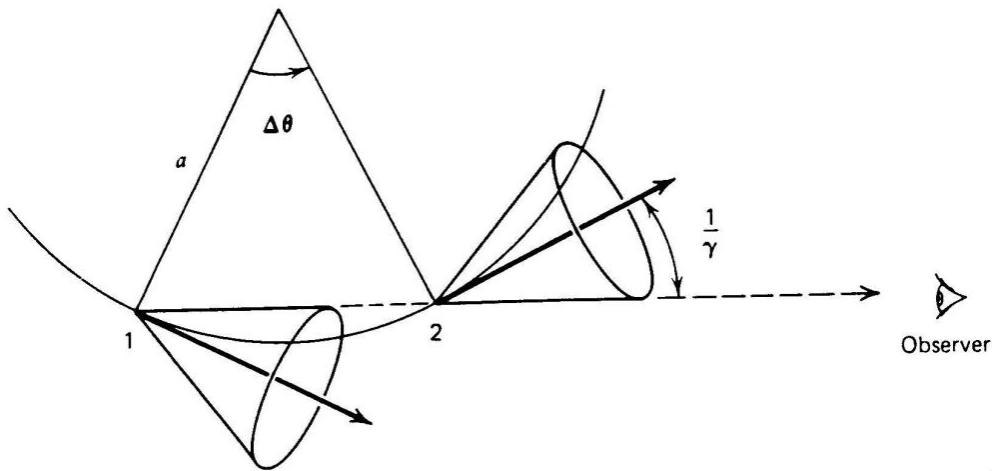


Figure 1.3.: Emission cones at various points of an accelerated particle's trajectory. Taken from Rybicki & Lightman (1979)

of electrons with energy in the range (E_1, E_2) where $n(E)dE$ is the number density of electrons with energy between E and $E + dE$. Then the emitted power by the electrons as a function of the frequency can be written as:

$$P(\nu) = \int_{E_1}^{E_2} P(E, \nu) n(E) dE \quad (1.2.10)$$

The observed radio spectra from emission region can be described with a power law form, so the number density of electrons for such a distribution can be expressed as:

$$n(E)dE = CE^{-p}dE \quad (1.2.11)$$

where C and p are constants.

The power per unit frequency per unit time as a function of frequency emitted by each particle is given by:

$$P(\omega) = \frac{\sqrt{3} q^3 B \sin \alpha}{2\pi mc^2} F\left(\frac{\omega}{\omega_c}\right) \quad (1.2.12)$$

with the critical frequency $\omega_c = \frac{3\gamma^2 q B \sin \alpha}{2mc}$ and $F(x) = x \int_x^\infty K_{5/3}(\eta) d\eta$ in which $K_{5/3}$ is the modified Bessel function of order $\frac{5}{3}$ and $x = \frac{\omega}{\omega_c}$. Combining this with Eq.1.2.10 and Eq.1.2.11 one can show that the synchrotron spectrum often can be approximated by a power-law over a limited range of frequency:

$$P(\nu) \propto \nu^{-a} \quad (1.2.13)$$

with $a = \frac{p-1}{2}$ as the spectral index and p as particle distribution index. One can conclude that the emitted spectrum from an electron power-law distribution is a power-law. Additionally if one consider extended radio sources, which are transparent to the synchrotron emission, then $\alpha \approx 0.5 - 1$ and thus $2 \lesssim p \lesssim 3$.

1.2.2. Synchrotron self-absorption

According to the principle of detailed balance, there is a corresponding absorption process to every emission process. For synchrotron radiation this process is called synchrotron self-absorption. This effect becomes important if the intensity of synchrotron radiation within a source becomes sufficiently high. This lead to a relationship for the flux density S_ν so that

$$S(\nu) = \frac{P(\nu)}{4\pi\alpha_\nu} \propto \nu^{5/2} \quad (1.2.14)$$

in which α_ν is the absorption coefficient and $P(\nu) = 2\pi P(\omega)$ is the emission power. The spectrum is shown in Fig.1.4 ²

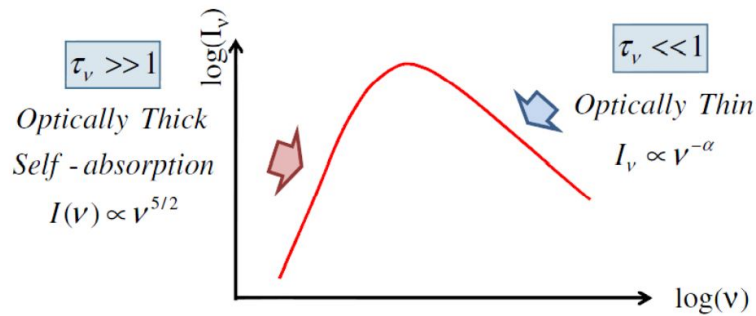


Figure 1.4.: Synchrotron spectrum from a power law distribution of electrons. Taken from AY121 - Radiative Processes in Astrophysics October 25, 2013

²https://sites.astro.caltech.edu/~mmanders/ay121/notes/Lecture_Slides_20131025_Gregg.pdf

As one can see in Fig.1.4 the above mentioned relationship Eq.1.2.14 apply for an optically thick medium ($\tau_\nu \gg 1$) which occur at low frequencies and create a cutoff of the spectrum. At higher radio frequencies, the medium becomes optically thin ($\tau_\nu \ll 1$) and the emission can be described by the power law given in Eq.1.2.13. Here, the optical depth τ_ν is given by:

$$\tau_\nu = \alpha_\nu l \quad (1.2.15)$$

in which l is the length of the optical medium. Spectra of this form are found in the nuclei of AGNs at radio, centimetre and millimetre wavelengths (Longair 2011).

1.2.3. High energy emission

The spectral energy distribution (SED) of blazars consists of two non-thermal emission humps see Fig.1.5. While the low-energy hump which peaks between infrared and X-rays can be described by synchrotron radiation, there are two different types of emission models explaining the high-energy hump which peaks at γ -rays from MeV to TeV, namely **leptonic** and **hadronic** emission models. Leptonic models suggest inverse Compton scattering between electrons/positrons in the jet and photons of their own synchrotron emission (synchrotron-self-Compton, SSC) or an external photon field e.g from the accretion disc (external-Compton, EC) as the responsible process. The inverse Compton scattering is the process, where low energy photons gain energy after a collision with ultra relativistic electrons. If the photons which participate in the inverse Compton scattering are produced by the electrons, which transfer the energy to these photons, it is called synchrotron self-Compton (SSC). In hadronic models, the low-energy hump is explained by the synchrotron emission of highly relativistic electrons. However, the high-energy emission is attributed to an additional component involving hadronic processes (Cerruti et al. 2017). A fraction of the kinetic power in the jet is used to accelerate protons, leading to the production of pions through interactions between photons and protons (Mannheim & Biermann 1992) (Mannheim 1993). This, in turn, generates an electromagnetic particle cascade. The acceleration of protons to these high energies necessitates the presence of strong magnetic fields, typically several tens of Gauss (Müller 2014). With this models it is also possible to explain neutrino emission of AGNs (Kadler et al. 2016). So, conducting extensive, multi-wavelength studies of the spectral energy distribution (SED) of active galactic nuclei (AGN) across a broad range of wavelengths, from radio to TeV energies, is crucial for analyzing potential scenarios and differentiating between various models.

1.3. Very Long Baseline Interferometry (VLBI)

If not mentioned otherwise, the following chapter is based on Burke et al. (2019). Because of the radio window of the Earth's atmosphere, we are able to observe the electromagnetic

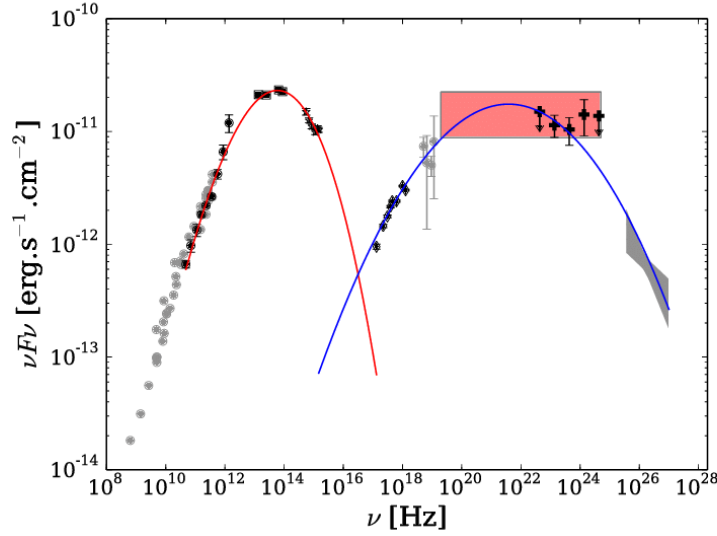


Figure 1.5.: Interpolation of the AP Lib SED by two third degree polynomial functions in red (synchrotron component) and blue (inverse Compton component). The red rectangle is the uncertainty area of the Compton peak position Taken from Hervet et al. (2015)

radiation in the radio band from the Earth's surface. The radio flux density S_ν is the relevant quantity which has to be determined. Its common unit is Jansky (Jy), which is the energy per time, surface area and frequency.

$$1\text{Jy} = 10^{-27} \left[\frac{\text{J}}{\text{s m}^2 \text{ Hz}} \right] \quad (1.3.1)$$

To analyze the structure of objects like AGNs one have to be able to resolve them. The angular resolution for a single dish telescope follows the Rayleigh criterion

$$\theta = 1.22 \frac{\lambda}{D} \quad (1.3.2)$$

Since we observe at a constant wavelength λ , the only chance to improve the resolution is to enlarge the diameter D of the telescope. The best way to do this is very long baseline interferometry (VLBI). In this technique one try to synchronizes multiple radio telescopes at the phase center of the antennas via baselines $\vec{b}_\lambda = \frac{\vec{b}}{\lambda}$ - the connection of the reflection centers of two telescopes. The baselines should be as large as possible for the best angular resolution. The simplest way to explain all important aspects of this technique is to have a look at a two element interferometer like it is shown in Fig.1.6.

1.3.1. Radio Interferometry

Two-element interferometer

Both antennas of the considered two-element interferometer are identical and point at a source under the direction $\vec{s} = \vec{s}_0 + \vec{\sigma}$, where \vec{s}_0 is the reference direction and $\vec{\sigma}$ is the distance from the center of the source to the center of the primary beam see Fig.1.6. The source is tracked by these two telescopes and one of them is selected as reference. There is a geometrical delay $\tau_g = \frac{\vec{b}\vec{s}}{c}$ when the signal arrives at the reference antenna. Additionally the second antenna also receives a instrumental delay τ_i to equalize the signals. If $\tau_g = \tau_i$, the reference direction \vec{s}_0 mentioned before is defined as phase tracking center. The cross-correlation $R_{xy}(\tau)$ - also called cross-power product since it has the dimension of power - over two amplitudes x and y is given by :

$$R_{xy}(\tau) := SA(\vec{s})\cos(2\pi\vec{b}_\lambda\vec{s}) \quad (1.3.3)$$

as time average of the multiplication of $x(t) = v_1\cos(2\pi\nu t)$ with $y(t-\tau) = v_2\cos(2\pi\nu(t-\tau))$, delayed by τ . S is the flux density of the source and $A(\vec{s})$ is the effective area of the antenna, which is smaller than the actual collecting area because in reality the total power will never be measured by a telescope. The output of an antenna from an observation of an object at a frequency ν corresponds to the output noise power of a black body at this frequency.

Another concept that uses the same measurement idea is the antenna temperature T_a . This is the temperature that a resistor would reach if it generated the same power density as the power density observed from the antenna port for any given frequency ν . The antenna temperature is given by:

$$T_a(\theta, \phi) = \frac{1}{\lambda^2} \int_{4\pi} T_b(\theta, \phi)A(\theta, \phi)d\Omega \quad (1.3.4)$$

Array of N-telescopes

Since the most measurements are taken place with more than two telescopes, it is useful to generalize the results above to an array of N telescopes. The fundamental equation for a practical interferometer is given by the complex visibility:

$$V_{i,j} = \int A(\sigma)B_\nu(\sigma)\exp(i2\pi\vec{b}_{i,j,\lambda}\sigma)d\Omega \quad (1.3.5)$$

The amplitude and the phase of this function are the principal observables in interferometry which can be measured with an array of multiple baselines $\vec{b}_{i,j}$ with an instrumental delay τ_i adjusted to the geometrical delay τ_g .

To get an relation between the complex visibility function $V_{i,j}$ and the brightness distribution $B_\nu(\sigma)$ of the observed source it is useful to introduce the right-handed rectilinear coordinate system (u, v, w). The w-direction can be defined with the unit

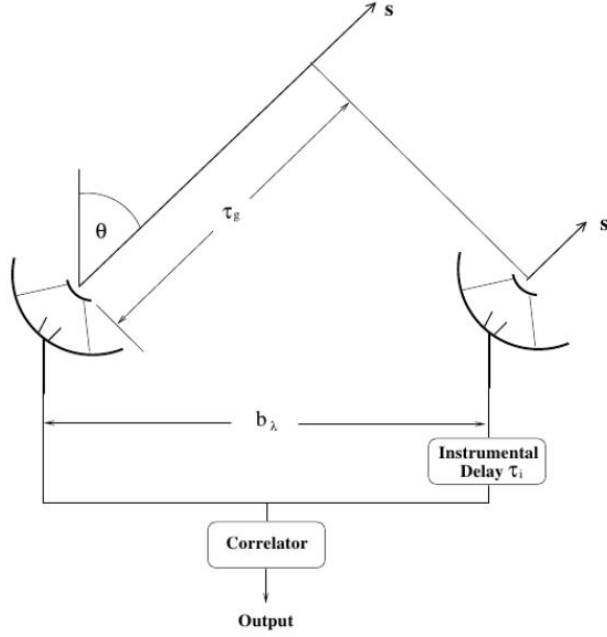


Figure 1.6.: The general structure of the two-element Michelson interferometer. Taken from Burke et al. (2019)

vector \vec{s}_0 which is perpendicular to the (u,v)-plane consisting of u, which is projected into the eastern direction and v, which is projected into the northern direction. The offset vector $\vec{\sigma}$ is parallel to the (u,v)-plane. With this assumption Eq.1.3.5 becomes

$$V_{i,j} = \int_{4\pi} A(l, m) B_\nu(l, m) \exp[i2\pi(ul + vm + wn)] d\Omega \quad (1.3.6)$$

where l,m,n are the direction cosines of the unit vector \vec{s} . So, (l,m) are the coordinates of $\vec{\sigma}$ and w=0 because \vec{s}_0 is perpendicular to the (u,v)-plane. With this consideration the solid angle $d\Omega$ can be written as

$$d\Omega = \frac{dl dm}{\sqrt{1 - l^2 - m^2}} \quad (1.3.7)$$

Since for most cases the offset angle σ is small, it is practical to rewrite Eq.1.3.5 in terms of the rectilinear coordinates for σ , x and y in the small angle approximation:

$$V(u, v) \approx \int A(x, y) B(x, y) \exp[2\pi i(ux + vy)] dx dy \quad (1.3.8)$$

With this introduced coordinate system one now can see that the visibility in the (u,v)-plane is the Fourier transform of a source's brightness distribution in the (x,y)-

plane

$$V(u, v) \xleftrightarrow{FT} B(x, y) \quad (1.3.9)$$

The biggest problem in practice is that it is not possible to cover the whole (u,v)-plane. Only a sample coverage is available.

$$V(u, v) \longrightarrow S(u, v)V(u, v) \quad (1.3.10)$$

where

$$S(u, v) = \sum_k \omega_k \delta(u - u_k) \delta(v - v_k) \quad (1.3.11)$$

where ω_k is the weighting factor.

The missing peaces in the (u,v)-plane lead to a loss of Fourier components in the synthesized image. One tries to fill up these components as far as possible with the so called aperture synthesis, where the Earth's rotation is used to cover the empty areas in the (u,v)-plane, which means that each pair of telescopes samples a trajectory of spatial frequencies as function of time. Such coverages depend on the position and the declination of the telescopes. For a declination of ± 90 deg the (u,v)-coverage would be circular whereas a coverage with a certain declination result in an elliptical geometry, e.g Fig.1.7.

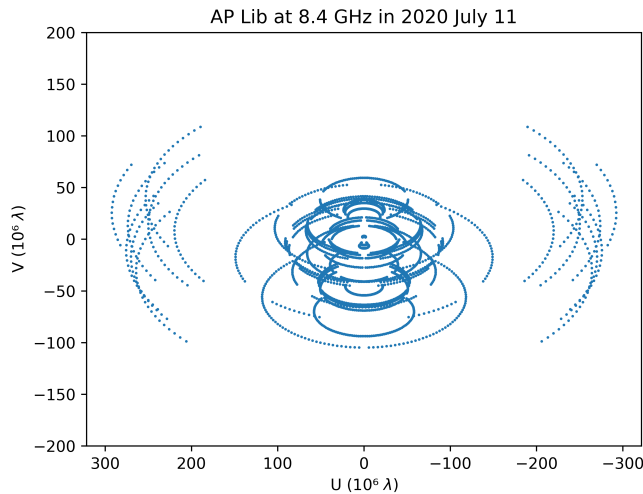


Figure 1.7.: (u,v)-coverage of AP Lib in July 2020

So to obtain the true brightness distribution one has to deconvolve the so called dirty image:

$$B^D(x, y) = \int S(u, v)V(u, v)\exp[-2\pi i(ux + vy)]dudv \quad (1.3.12)$$

applying Eq.1.3.11 one gets:

$$B^D(x, y) = \sum_k V(u_k, v_k) \omega_k \exp[-2\pi i(u_k x + v_k y)] \quad (1.3.13)$$

With the convolution theorem one gets

$$B^D = P^D * B \quad (1.3.14)$$

with

$$P^D = \int S(u, v) \exp[-2\pi i(ux + vy)] du dv \quad (1.3.15)$$

which equals:

$$P^D = \sum_k \omega_k \exp[-2\pi i(ux + vy)] \quad (1.3.16)$$

where the so called dirty beam P^D is equivalent to a point spread function.

The conclusion is that if one wants to get the real brightness distribution one have to deconvolve the dirty image B^D which will be done in Sec.2.

1.3.2. Disturbance effects

While measuring the source multiple effects can appear which can strongly disturb the receiving signal. An ideal radio telescope would only detect radiation from the line of sight, whereas the sensitivity of a real parabolic radio telescope has an angle dependency with its maximum in the direction of the line of sight. This direction is called main beam. Additionally there is detected radiation from outside the observing direction - which can be described by the side lobes. Especially if a additional source that is not to be observed is located in the direction of the observed source this disturbance effect becomes important. Another important aspect is scattering. The incoming waves can be scattered at the feedhorn and its mounting and therefore the signal can be worsen. Furthermore there is radio frequency interference (RFI) which is caused by unwanted signals, e.g artificial/man made signals and can eventually superimpose the signal. Moreover there is the so called spillover effect, where the signal skips the first focus and reaches the secondary focus directly.

1.3.3. VLBI monitoring programs

MOJAVE

A concrete VLBI-array which was used to obtain the data for this work is the Very Long Baseline Array (VLBA). It consisting of 10 identical antennas with a size of 25m which are separated by distances from 200km to transcontinental baselines of 8600 km. To

visualize: The longest baseline is between Mauna Kea, Hawaii and St. Croix, Virgin Islands. One application is a long term program which was created for observations of AGN jets of the northern sky at frequencies of 15 GHz, 23 GHz and 43 GHz is MOJAVE (Monitoring Of Jets in Active galactic nuclei with VLBA Experiments). According to the MOJAVE team the major aims of the program are to deliver much improved image resolution, size, and statistical completeness in comparison to previous surveys as well as to analyze the temporal behaviour of the kinematics and polarization and find out how these properties are related to other source properties. The complete MOJAVE sample include - after multiple additions since 1994, like the newest "MOJAVE 1.5 Jy quarter century sample" from Lister et al. (2019) - 409 AGNs observed at 15GHz with the VLBA in a period between 1994 and 2019. The size of the dataset makes the sample the largest and most complete radio-loud blazar sample to date, covering 75 % of the entire sky. The selection criteria is that the total 15GHz VLBA flux density exceeds 1.5 Jy at any epoch between 1994.0 and 2019.0.

TANAMI

TANAMI (Tracking Active Galactic Nuclei with Austral Milliarcsecond Interferometry), is a multiwavelength program to monitor relativistic jets in AGN of the Southern Sky. From 2007 until 2020 TANAMI observed source with only -30° declination. The measurements took place at frequencies 8.4 and 22.3 GHz, which allows to measure spectral indices of jet features and their time evolution (Kadler et al. 2015). Since 2020 on, the program was extended to the whole southern sky and the observations take place at 8.4 and 2.3 Ghz. This array include multiple telescopes consisting of the LBA (Australian long baseline array) which is made of 5 telescopes, Hartebeesthoek, South Africa, and the 34 m and 70 m telescopes of the NASA Deep Space Network in Tidbinbillaan. Additionally there are two AuScope antennas in Yarragadee, Western Australia and Katherine Northern Territory and a telescope in Warkworth, New Zealand. This array is complemented by a radio flux-density monitoring program with the ATCA (Australia Telescope Compact Array) at frequencies of 4.8, 8.6, 17/19, 38 and 40 GHz and a single-dish monitoring program using the University of Tasmania telescope at Ceduna. At 6.7 GHz, the Rapid Eye Mount (REM) telescope to cover the NIR/optical part of the spectrum, the Fermi Large Area Telescope (LAT) - monitoring the sky at 30 MeV to 300 GeV see Tab.1.2.

1.3.4. Jet kinematics

One of the first results after the implementation of VLBI in radio astronomy in the late 1960s and early 1970s, was that some AGNs consisted of more than one component. These components seem to move with superluminal speeds (speeds higher than speed of light), which seem to be unphysical. By means of the model of Rees (1966), it will be shown that **superluminal motion** can be explained as an optical illusion caused by an

1. Theoretical background

Telescope Name	Diameter (meters)	Location
Parkes	64	Parkes, New South Wales, Australia
ATCA	5×22	Narrabri, New South Wales, Australia
Mopra	22	Coonabarabran, New South Wales, Australia
Hobart	26	Mt. Pleasant, Tasmania, Australia
Ceduna	30	Ceduna, South Australia
Hartebeesthoek	26	Hartebeesthoek, South Africa
Warkworth	12	Auckland, New Zealand
Katherine	12	Northern Territory, Australia
Yarragadee	12	Western Australia

Table 1.2.: The TANAMI array

object moving partly in the direction of the observer. This section is based on Kembhavi & Narlikar (1999) and Carroll & Ostlie (2017) if not mentioned otherwise. Imagine a relativistic jet moves with speed v (actual speed of the source) towards an observer at point O as illustrated in Fig.1.8. At time t_1 a signal is emitted from point A. At time $t_2 = t_1 + \Delta t$ a second signal is emitted from point B. The signals arrive at the observer at t'_1 and t'_2 . The angle ϕ is small enough that the two luminosity distances named D_L are approximately the same. The first signal reaches the observer after $t'_1 = t_1 + \frac{D_L + v\Delta t \cos\theta}{c}$. The second arrives at $t'_2 = t_2 + \frac{D_L}{c}$. The time between the reception of the two signals is therefore:

$$\Delta t' = t'_2 - t'_1 = t_2 - t_1 - \frac{v\Delta t \cos\theta}{c} = \Delta t(1 - \beta \cos\theta) \quad (1.3.17)$$

with $\beta = \frac{v}{c}$, which is shorter than Δt . Considering that:

$$BC = D_L \sin\phi \approx \phi D_L = v\Delta t \sin\theta \quad (1.3.18)$$

$$\phi D_L = v \sin\theta \frac{\Delta t'}{1 - \beta \cos\theta} \quad (1.3.19)$$

The apparent transverse speed measured at the point O is:

$$v_{app} = \frac{\phi D_L}{\Delta t'} = \frac{v \sin\theta}{1 - \beta \cos\theta} \quad (1.3.20)$$

which leads to superluminal motion for large β and small θ . v_{app} can be rewritten to:

$$\beta_{app} = \frac{v_{app}}{c} = \frac{\beta \sin\theta}{1 - \beta \cos\theta} \quad (1.3.21)$$

Whenever a signal moves with relativistic speed ($\gamma \gg 1$) the **relativistic beaming**

effect, which was discussed in Sect. [1.2.1] becomes important. It has an affects to the morphology of an AGN, since because of this effect a two-sided source can appear one-sided. This became clear when one consider that if S_ν is the flux density, than S_ν/ν^3 is invariant under Lorentz transformation see (Rybicki & Lightman 1979). Since $S_\nu \propto I(\nu)$ the observed intensity of a moving jet component which follow a power law ($I(\nu) = A\nu^\alpha$) reads:

$$I(\nu_{obs}) = \delta^3 A \nu_{emit}^\alpha = \delta^3 A \delta^{-\alpha} \nu_{obs}^\alpha \quad (1.3.22)$$

which can be rewritten into:

$$I(\nu_{obs}) = \delta^{3-\alpha} I(\nu_{emit}) \quad (1.3.23)$$

where δ is the so called relativistic Doppler factor:

$$\delta = \frac{\sqrt{1 - \beta^2}}{1 - \beta \cos(\theta)} \quad (1.3.24)$$

So if one combine Eq.1.3.24 and Eq.1.3.23 one obtain for the ratio of the observed fluxes:

$$\frac{S_{jet}}{S_{counter}} = \left(\frac{1 + \beta \cos \phi}{1 - \beta \cos \phi} \right)^p \quad (1.3.25)$$

where $p = (3 - \alpha)$ for observations of multiple components and $p = (2 - \alpha)$ for observations of jets which can be expressed as a series of components. These considerations are based on ?.

1.3.5. DIFMAP

As it was shown in chapter 1.3.1, one have to deconvolve the Fourier tranformed sampling function (dirty beam) to get the real brightness distribution. According to the DIFMAP COOKBOOK (Taylor 1994) this can be done by means of the iterative CLEAN algorithm implemented in the program DIFMAP as follows: First one has to choses weighting. Either one chose the natural weighing where all the data is weighted equally, or uniform weighting, where the data is weighted inversely to the number of visibilities. The next step is to open up the so called dirty map (observed brightness) and find the brightest region. Around that region one has to set windowns in which the CLEAN algorithm subtract the dirty beam multiplied by the peak strength and a damping factor - usually called loop gain - from the dirty image, at the position of the peak. This has to be repeated, considering that each time the dirty map has to be replaced with the remaining map from previous iteration until the intensity of the peak is no longer significant in comparison to the general noise level of the map. At the end one gets an image with less influence from the side lobes and sampling, the so called - clean image. These cleaned images had to be modelfitted to obtain Gaussian distribution models of the

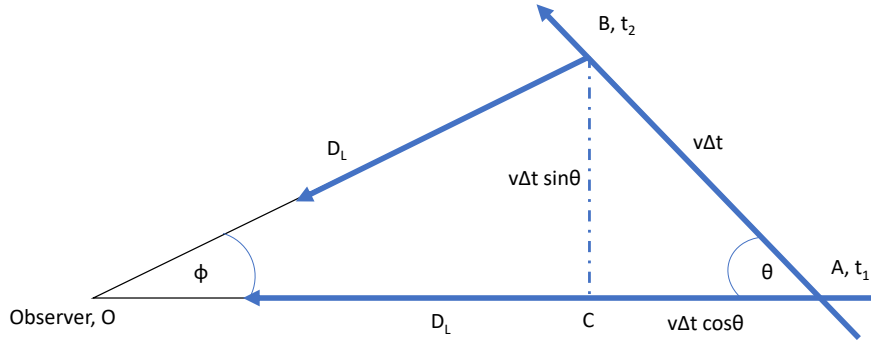


Figure 1.8.: Illustration of the above mentioned calculations to derive the apparent velocity.

emission regions within the jet. Such models help to track components or brightness temperatures of the jets for example. To do this, one uses the modelfit algorithm. Around the brightest spot which is the core of the jet, one define a Gaussian. Here, one uses a elliptical gaussian whereas all the other components get circular gaussians. The algorithm fits the component to the emission region and subtracts the component flux from the map. This allows to find additional emission regions which are also fitted with Gaussians. This has to be iterated until the background is homogeneous and the Gaussian model describe the source's emission regions well enough.

2. Data analysis

2.1. Data preparation and modelfitting

The motivation for this thesis is as follows. There is existing data of AP Lib from the MOJAVE program - including observations from August 1997 until May 2012. The TANAMI program started to observe AP Lib again in 2020 since the selection criteria for the program were changed from sources located at declinations south of -30 degree to sources from the whole Southern sky. One of the main tasks now is to close this 8 year observational gap via simulations, meaning that existing data is extrapolated to create synthetic TANAMI visibility data for that date at which AP Lib was observed by TANAMI for the first time. For this purpose, the python modul ehtim ¹ was used which requires certain input parameters, namely: position, flux density and size of the jet components. In the following, it is explained how these values are obtained. First the clean data files were downloaded from the MOJAVE homepage ². All 22 epochs were modelfitted with 2D Gaussian components using the program DIFMAP, as described in Sec.1.3.5. According to Lister et al. (2019) the relative uncertainties of the components' parameters were chosen to be: 20% for the relative uncertainties of the major and minor axes and 5% for the relative uncertainties of the flux density which, however, could be much larger for cases in which several components are located very close to each other. The corresponding plot and modelfit parameters are shown for every epoch in Appendix A. Some of these components' minor or major axis diverge. So the resolution limit was computed for every component following Kovalev et al. (2005) to see which components are not resolved. These were neglected for the estimation of the size of the components which will be explained in the following sections.

$$\theta_{lim} = b_{\psi} \sqrt{\frac{4 \cdot \ln(2)}{\pi} \cdot \ln\left(\frac{\text{SNR}}{\text{SNR} - 1}\right)} \quad (2.1.1)$$

The term b_{ψ} represents the size of the observational beam measured along a specific position angle ψ .

In the case of the elliptical core components, resolution limits for their minor and major axis were calculated. Here, ψ is given by the position angles of the corresponding minor and major axis of the fitted Gaussian component, respectively. For the circular

¹<https://achael.github.io/eht-imaging/>

²<https://www.cv.nrao.edu/MOJAVE/sourcepages/1514-241.shtml>

jet components the major axis of the corresponding beam was used for b_ψ .

The SNR or Signal-to-Noise Ratio is calculated as

$$\text{SNR} = \frac{S_{core}}{\sigma_{core}} \quad (2.1.2)$$

Here, σ_{core} refers to the noise level within the area of the image that corresponds to the component, while S_{core} represents the flux density of the component.

θ_{lim} represents the upper limit for the size of the minor and major axes of the corresponding core component. If an axis is smaller than the corresponding θ_{lim} value, it is considered unresolved.

The brightness temperature was calculated corresponding to Kovalev et al. (2005):

$$T_b = \frac{2 \ln 2 S \lambda^2 (1 + z)}{\pi k \theta_{maj} \theta_{min}} \quad (2.1.3)$$

where S is the flux density of the corresponding component, λ is the wavelength of the observation (here corresponding to 15 GHz), z is the redshift (0.049 for AP Lib³) and θ_{maj} and θ_{min} are the major and minor axes of the corresponding component, respectively. The results are shown in Fig.2.1.

In the following the resulting components were cross identified through all the epochs. This process is one of the crucial points of this work, since there are uncertainties and therefore multiple possibilities to identify the components, which results in different simulation predictions.

In this thesis, two different identification models are tested. In both cases the core component was assumed to be stationary and the distances of all the other components were measured with respect to it.

The flux density S was fitted according to:

$$S = a_x + b_x \cdot t \quad (2.1.4)$$

where t is the time and a_x and b_x are fitting parameters.

2.1.1. Kinematic analysis

To study the time evolution of the positions of the jet components, a vectorial kinematic analysis was performed by means of the following equations, following Lister et al. (2019).

$$x(t) = x_{mid} + \mu_x \cdot (t - t_{mid}) \quad (2.1.5)$$

in which $x(t)$ and $y(t)$ are the position of the component in RA and Dec direction, respectively

³<https://www.cv.nrao.edu/MOJAVE/sourcepages/1514-241.shtml>

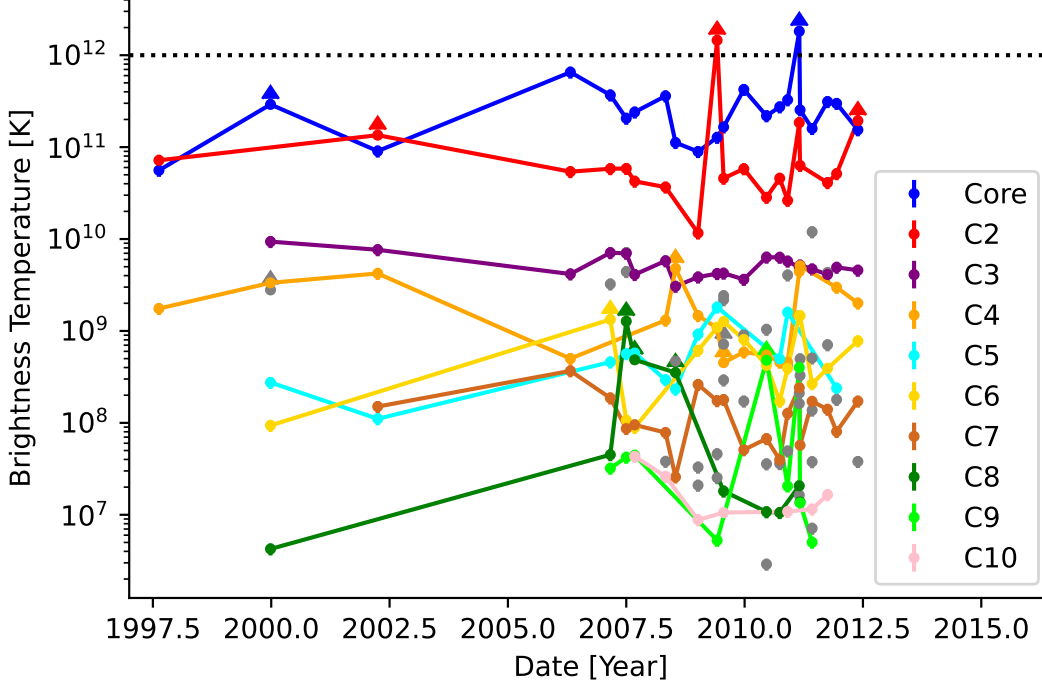


Figure 2.1.: Brightness temperature over time for each component of every epoch. The inverse Compton limit is indicated through the dotted line.

$$y(t) = y_{mid} + \mu_y \cdot (t - t_{mid}) \quad (2.1.6)$$

in which μ_x and μ_y are the angular speeds in RA and Dec, $x(t)$ and $y(t)$ are the position of the component in RA and Dec direction, x_{mid} and y_{mid} are the position of the component in RA and Dec direction at the time t_{mid} , respectively and t_{mid} is the midpoint of observation.

$$t_{mid} = (t_{min} + t_{max})/2 \quad (2.1.7)$$

The resulting vector modulus is:

$$\mu = \sqrt{(\mu_x^2) + (\mu_y^2)} \quad (2.1.8)$$

The apparent speed in units of the speed of light c with D_L as the luminosity distance reads:

$$\beta_{app} = \mu \cdot D_L / c(1 + z) \quad (2.1.9)$$

The last parameter which is needed for the simulation and got to be interpolated is the corresponding size s of the components. This quantity was fitted according to Rösch et al. (2022) with:

$$s = c \cdot (r + d)^l \quad (2.1.10)$$

where c is the fitting parameter, r is the distance of the 15 GHz core component to the jet base and l the power law index defining the jet geometry ($l = 1$ for a conical jet, $l < 0$ for a collimated jet, and $l > 0$ for a decelerating jet according to Kadler et al. (2004)).

$$d = \sqrt{x(t)^2 + y(t)^2} \quad (2.1.11)$$

2.2. Simulation

The simulation was done with the `ehtim` package which is a python module designed for manipulating, simulating and reconstructing VLBI data. In this thesis synthetic data was produced with a Gaussian model (elliptical core, rest circular) representing the AP Lib in 2020. To create synthetic data, the program requires the components as input of the corresponding model together with their position, size and flux densities. Additionally one has to provide an observational telescope array. AP Lib was observed with the LBA in 2020, so this array (see Tab.2.1) was used as initial input array. Beside this priors the observation date was set to 2020-07-11 since the TANAMI observations took place on this day, the observed frequency to 8.4 GHz (the observational frequency of the TANAMI program). Normally, the TANAMI observations are scheduled with 6 scans with a duration of 10 minutes of each scan, which results in 1 hour of observation per source. Such a observation was not possible in `ehtim`, since the gaps had to be equidistant. Also considering that there was no big difference in the simulation results from 24 hour and e.g 5 hour observation, the duration of the observation was set to 24 hours. Although the mentioned telescopes have an individual elevation limits, the elevation range went from 10 to 80 (default settings) degrees for all telescopes since it was not possible to set these limits one by one. However, this should not influence the simulation drastically. Even though it was possible to image the resulting synthetic visibilities directly through `ehtim`, the data was imaged through DIFMAP whose imaging process is based on the CLEAN algorithm described earlier since there was no concrete preference and it is also not the main part of this thesis to focus on.

Telescope	X [m]	Y [m]	Z [m]	SEFD[Jy]
ATCA	-4751639.85972	2791700.3567	-3200491.11339	72
Mopra	-4682769.0585	2802619.04217	-3291759.33837	430
Parkes	-4554232.7408	2816758.859	-3454034.6988	43
Hobart	-3950237.6192	2522347.7349	-4311561.5974	590
Ceduna	-3753442.7457	3912709.753	-3348067.6095	600
Hartebeesthoek	5085490.8071	2668161.6274	-2768692.5007	340
Katherine	-4147354.8905	4581542.2955	-1573302.8297	3400
Yarragadee	-2388896.4538	5043350.0584	-3078590.5092	3400
Warkworth	-5115324.572	477843.277	-3767192.6092	650

Table 2.1.: List of telescopes used for the simulation. X, Y, Z are the coordinates of the telescopes with respect to the center of the Earth and SEFD is the system equivalent flux density of the telescopes.

3. Results

In this chapter the methods introduced in Chapter.2 were applied on concret models which will be explained and presented in the following. Cleaned data from the MOJAVE sample was modelfitted with 2D Gaussian components. These resulting components were cross identified throughout all the epochs. This process is one of the crucial points of this work, since there are uncertainties and therefore multiple possibilities to identify the components, which results in different simulation predictions. The cross identification throughout all epochs resulted in two different models namely one with only stationary components (model stat) and one with stationary and moving components (model mov) which are shown in Fig.3.1. In both cases the core component was assumed to be stationary and the distance of all the other components was measured with respect to it.

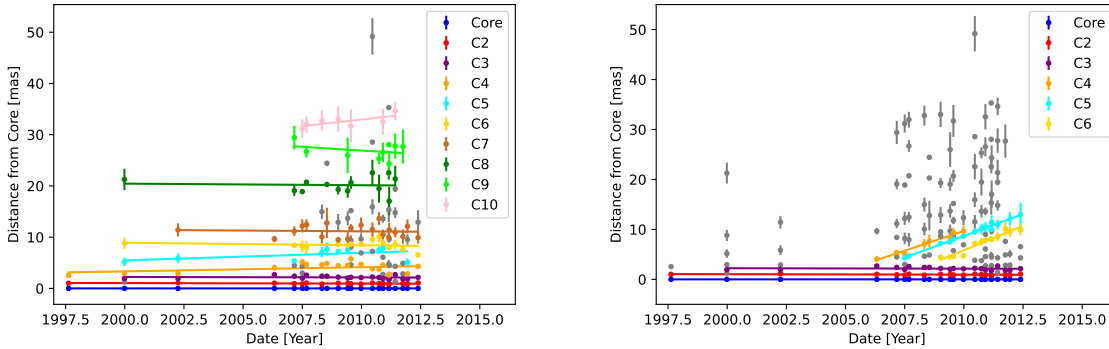


Figure 3.1.: Cross identification of Gaussian components resulting in only stationary features (left) and cross identification of Gaussian components resulting in stationary and moving (C4,C5,C6) features (right). The lines are fitted via vectorial linear regression and their gradient represents the component’s angular speed. The error bars are estimated by the major axis of the corresponding component.

The corresponding speeds are shown in Tab.3.1 and Tab.3.2.

The light curves of the components, in which their flux density is shown with respect to the observation date, are also useful to cross identify the components. One expect that the flux density of a component remains constant in time or decreases significantly with time, which can be seen Fig.3.2.

The size of the components was extrapolated by means of Fig.3.3.

3. Results

Component	$(\mu_{stat} \pm \sigma_{\mu,stat})$ [mas/year]	$\beta_{app,stat} \pm \sigma_{\beta_{app,stat}}$
Core	0.000 ± 0.056	0.000 ± 0.210
C1	-0.009 ± 0.065	-0.034 ± 0.244
C2	-0.008 ± 0.072	-0.032 ± 0.268
C3	0.082 ± 0.058	0.306 ± 0.218
C4	0.148 ± 0.087	0.556 ± 0.325
C5	-0.049 ± 0.087	-0.183 ± 0.327
C6	-0.031 ± 0.095	-0.115 ± 0.355
C7	-0.031 ± 0.096	-0.116 ± 0.359
C8	-0.291 ± 0.210	-1.089 ± 0.785
C9	0.513 ± 0.267	1.922 ± 1.001

Table 3.1.: Speed of the components of the stationary model, where μ_{stat} is the angular speed of the components, $\beta_{app,stat}$ the apparent speed in units of the speed of light.

Component	$(\mu_{mov} \pm \sigma_{\mu,mov})$ [mas/year]	$\beta_{app,mov} \pm \sigma_{\beta_{app,mov}}$
Core	0.000 ± 0.056	0.000 ± 0.210
C1	-0.009 ± 0.065	-0.034 ± 0.244
C2	-0.008 ± 0.072	-0.032 ± 0.268
C3	1.579 ± 0.294	5.912 ± 1.101
C4	1.744 ± 0.188	6.530 ± 0.705
C5	1.972 ± 0.279	7.382 ± 1.046

Table 3.2.: Speed of the components of the moving model, where μ_{stat} is the angular speed of the components, $\beta_{app,stat}$ the apparent speed in units of the speed of light.

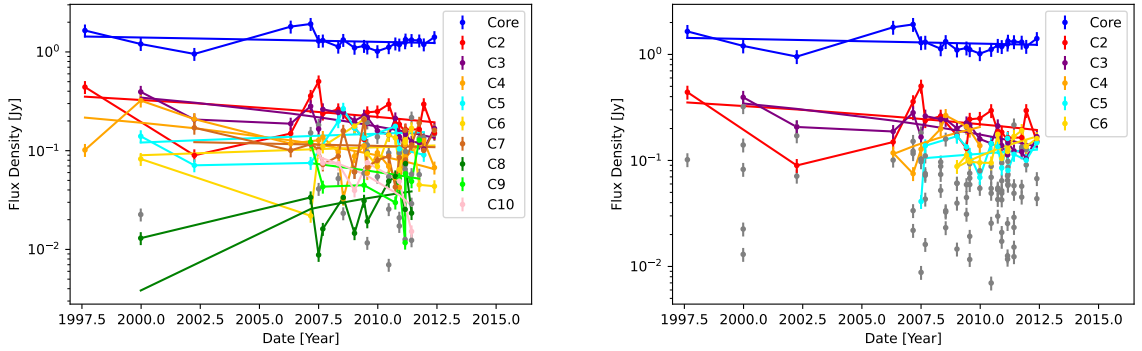


Figure 3.2.: Flux fits according to eq.2.1.4 for each component of the model with only stationary features (left) and Flux fits according to eq.2.1.4 for each component of the model with stationary and moving features (right).

So, if one gather everything together (including the plots for the size of the compo-

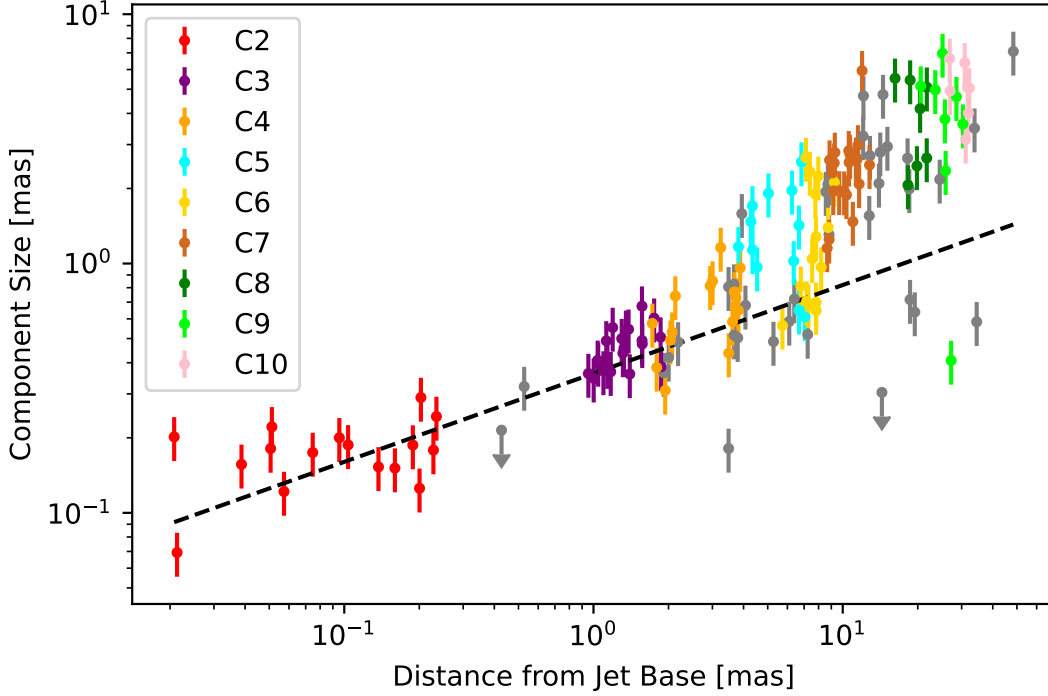


Figure 3.3.: Component size over distance from the jet base fitted according to Eq.2.1.10. The dashed line represents the mean component size as a function of the distance computed by linear regression, neglecting the diverging components. The arrow down signs represent the upper limits of the corresponding components. Every component was assigned to one color. The unidentified components are grey.

ments) prepared data can be simulated. The final simulation parameters were extrapolated from all the plots shown in this section and are shown in Tab.3.3 and Tab.3.4.

As one can see in Tab.3.3 and Tab.3.4, although there were initially 10 components for the model showing only stationary components and 6 for the moving one, only 7 and 4 components were used for the simulations, respectively, since for some components the extrapolation of the flux density resulted in negative values. These components were therefore excluded from the simulations and labeled as non existent at the simulated epoch. Also the values for the corresponding parameters are consistent with the theory because one expect that the most flux density is from the core component and the further away a component is the the fainter it gets - that means less flux density - and it gets also larger what results in greater values for the major axes.

Using the simulation parameters listed in Tab.3.4 and Tab.3.3 in combination with the telescope array described in Sec.2.2, one obtains the simulated images shown in Fig.3.4.

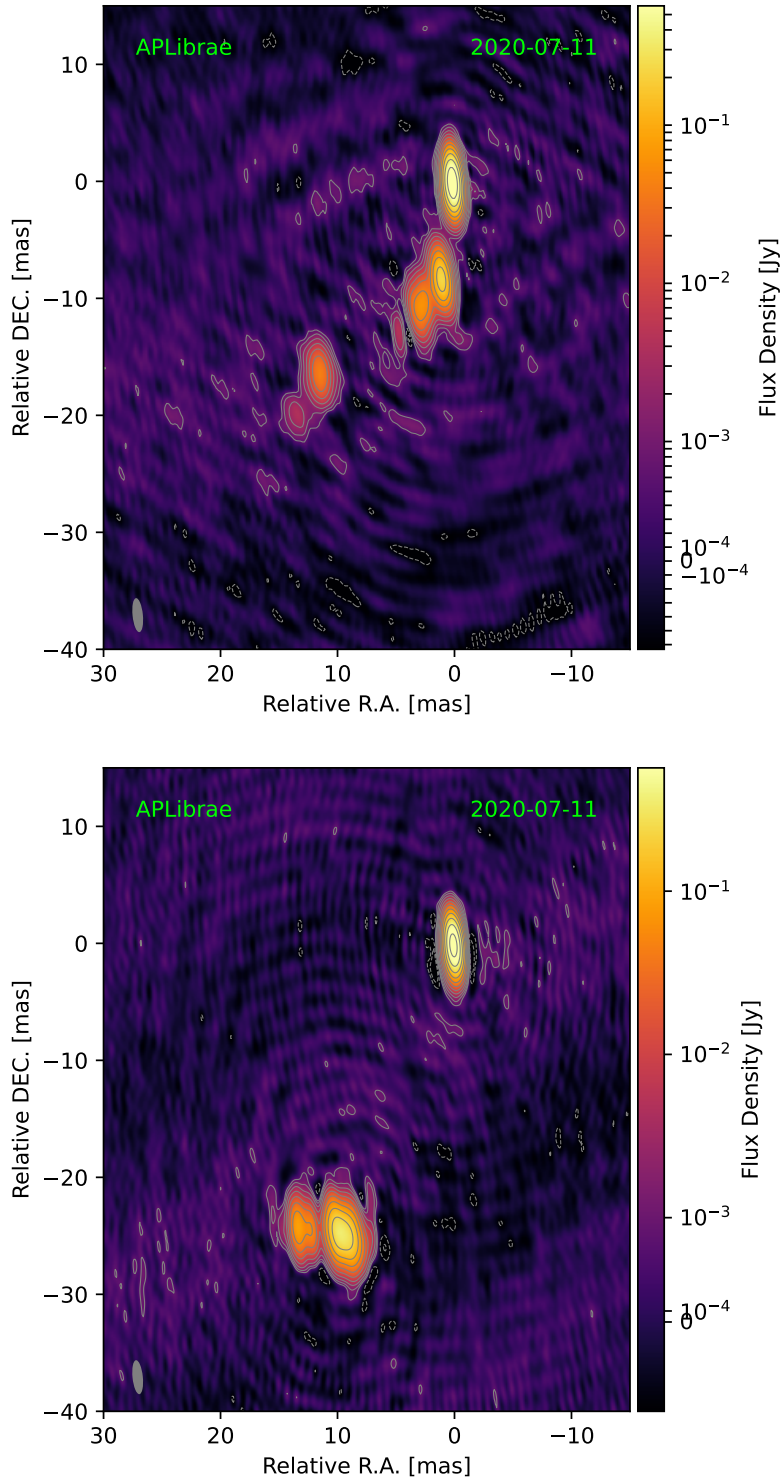


Figure 3.4.: Naturally weighted clean image of the simulated visibilities of the stationary (upper image) and moving (lower image) model. The contours start at 3σ and increase logarithmically with a factor of 2. The gray ellipse in the bottom left corner corresponds to the beam.

Component	Flux density [Jy]	Major Axis [mas]	Minor Axis [mas]	Theta [deg]	x [mas]	y [mas]
Core	1.12	0.50	0.073	-13.44	0	0
C1	0.11	0.67	0.67	0	0.20	-0.93
C2	0.18	0.75	0.75	0	0.95	-8.59
C3	0.13	0.73	0.73	0	1.07	-7.94
C4	0.10	0.82	0.82	0	2.75	-10.56
C5	0.07	1.03	1.03	0	11.34	-16.38
C6	0.0084	1.10	1.10	0	13.39	-19.88

Table 3.3.: Simulation parameters of each stationary component with flux density, major and minor axis, theta is the position angle of the component centroid from the assigned phase center in degrees east of north and x and y are the positions of the components from the core.

Component	Flux [Jy]	Major Axis [mas]	Minor Axis [mas]	Theta [deg]	x [mas]	y [mas]
Core	1.12	0.50	0.073	-13.44	0.0	0.0
C1	0.11	0.11	0.11	0.0	0.28	-0.81
C2	0.47	1.14	1.14	0.0	9.91	-24.42
C3	0.16	1.16	1.16	0.0	13.01	-24.20
C4	0.36	1.15	1.15	0.0	8.90	-25.18

Table 3.4.: Simulation parameters of each stationary and moving component with flux density, major and minor axis, theta is the position angle of the component centroid from the assigned phase center in degrees east of north and x and y are the positions of the components from the core.

4. Discussion

As it was pointed out in the previous chapters, cleaned data from the MOJAVE sample was used in this thesis. The MOJAVE team did a parsec-scale jet kinematics study of 409 AGNs based on 15 GHz Very Long Baseline Array (VLBA) data obtained in a 18 year span (between 1994 August 31 and 2016 December 26) as part of the 2 cm VLBA survey (Lister et al. 2019). AP Lib was one of the mentioned sources. This source is interesting concerning its jet geometry as one could see in Fig.3.3. The slope of the the FWHM component size function is $l = 0.35 \pm 0.015$ but at roughly 1 mas from the core the slope change to approximately $l=1$. This means that the jet geometry changes from parabolic ($l \approx 0.5$) to a conical ($l=1$) shape which can be interpreted as a change from a collimated jet to a more freely expanding jet Burd et al. (2022). This can be understood as the change of the pressure gradient of the external medium at the geometry transition point. The region where one expect a change of the pressure gradient of the external medium is called Bondi-sphere (Burd et al. 2022). Such transitions were already observed in many cases. For example, it was shown by Asada & Nakamura (2012) that such a geometry transition can be observed in the vicinity of the Bondi-sphere. As it was already mentioned in Sec.3 there are multiple possibilities to cross identify the modelfitted components. In this thesis two of the possibilities were analyzed. The MOJAVE team identified 3 moving components which are comparable to the moving components of the model showing stationary and moving components (model mov) from Sect.3 (see also Fig.4.1). As one can see in Tab.3.2 where the speeds of this model are listed, especially components C4, C5, C6 have non vanishing speeds within their 3σ uncertainties whereas the inner two jet components close to the core component remain stationary. The components from outer regions remained unidentified since in this model they seem to be unreliable, meaning that these components appear and disappear in several consecutive epochs or are too delocalized. It is also more useful to concentrate on the inner regions around the core because the in blazars one expect that most flux density is originated from the core region. The further away from the core, the larger and fainter it will become, which can be seen in Tab.3.4 in the columns "Major Axis" and "Minor Axis" and "Flux density", respectively.

This is consistent with the existing theory of jets. The corresponding final simulation image to this model can be seen in Fig.3.4. As one would expect from a model with moving components, in the 8 year which were unknown since MOJAVE ended the observation of AP Lib in 2012 and TANAMI started it in 2020, the simulation reveals that the moving components traveled downstream the jet and are located farther away from the core component compared to the last MOJAVE observation in 2012

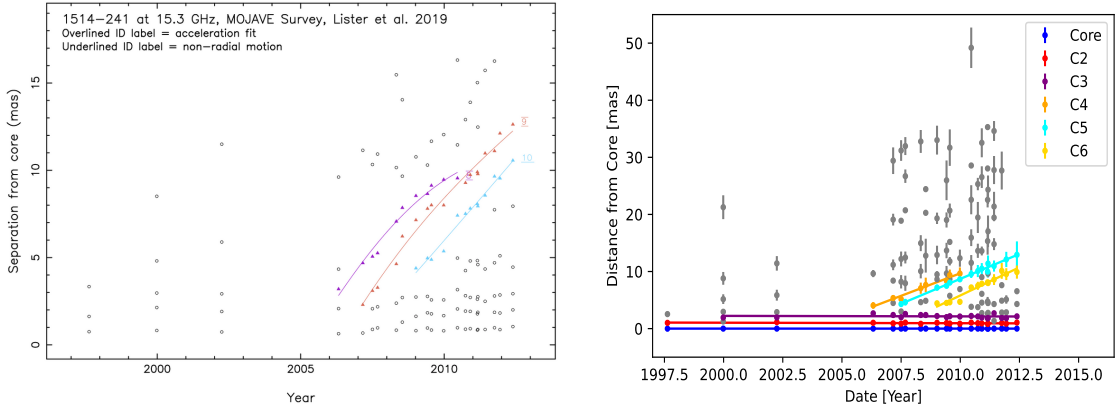


Figure 4.1.: Cross identification of Gaussian components from the MOJAVE team (left) resulting in 3 moving components and cross identification of Gaussian components resulting in stationary and moving (C4,C5,C6) features (right). The lines are fitted via vectorial linear regression and their gradient represents the component’s angular speed. The error bars are estimated by the major axis of the corresponding component.

The other possible model is with stationary features only. The comparison to the model presented by the MOJAVE team is shown in Fig.4.2. One can see by eye that the cross identification which leads to stationary components only is also possible in the MOJAVE team version. The speeds of the stationary model are shown in Tab.3.1. Each component’s angular and apparent speeds are consistent with stationary components within their 3σ uncertainties. This means that the speed are comparable with 0 within these uncertainty intervals. The plots of the components’ flux density shown in Fig.3.2 confirm that such a cross identification is also legit. Similar to the model with moving features the development of the flux density and the size of the components make sense. is reasonable. The component which is most distant from the core component is the largest one and shows the lowest flux density (see Tab.3.3). The corresponding final simulation image can be seen in Fig.3.4.

Both models are valid since the process of the cross identification is subject to uncertainties. This, however, leads to different prediction models which are shown in Fig.3.4. The obvious difference is that in the moving model there are two bright features farther downstream of the jet corresponding to the moving components C4, C5 and C6 shown in Fig.4.1. These features are not present in the stationary model. The most distant component of the stationary model seem to disappear in the moving model. This also can be explained with its velocity. The outermost component moves downstream the jet and becomes fainter and fainter so that it is not longer detectable. The moving model also shows no components close to the core region which is because the model does not include the ejection of further jet components. One would expect that new jet components would be ejected during flaring states of AP Lib which would lead to a similar jet

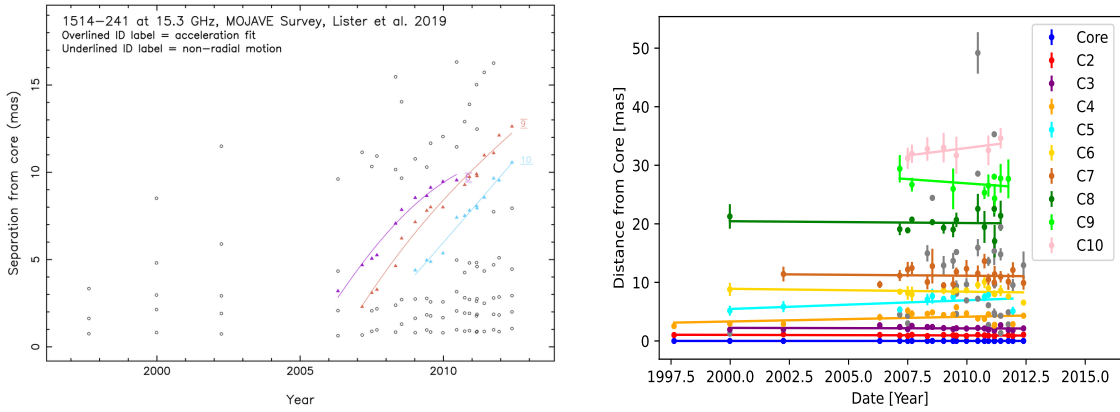


Figure 4.2.: Cross identification of Gaussian components from the MOJAVE team (left) resulting in 3 moving components and cross identification of Gaussian components resulting in only stationary features (right). The lines are fitted via vectorial linear regression and their gradient represents the component’s angular speed. The error bars are estimated by the major axis of the corresponding component.

structure close to the core region as shown for the stationary model. At this point there is no preference which model would rather describe the situation of the source in the year 2020. It remains to wait for the calibration of the measured data which will reveal which model corresponds to the actual observational data. What the final comparison with the actual data would imply for each model and what would be the next steps will be discussed in the following chapter.

5. Conclusion and Outlook

AP Lib was observed from August 1997 until May 2012 by the MOJAVE program. Then the observations stopped which resulted in a 8 year observational gap until the TANAMI program started the monitoring of the source since it was extended to the whole Southern sky (before only source with declination of -30°). One of the main points of this work was to close this gap by means of simulations to compare these simulated data with the real observational data from 2020. The simulation results can also help by imaging the data since the position of the components is basically known. For this purpose, fully calibrated and imaged data files of 22 epochs were downloaded from the MOJAVE homepage ¹ and modelfitted with 2D Gaussian components using the program DIFMAP. These modelfitted components were cross identified through all epochs. Based on this cross identification the dataset was set up for simulation by doing a kinematic analysis as well as a component's size and flux density extrapolation which was described in Sec.2. These extracted parameters in combination with the corresponding telescope array (LBA) were required to create synthetic data with the python tool ehtim. As one can see, the final result depends on the cross identification which is one of the first steps of this procedure and also the most crucial part of the thesis and its problematic. Depending on how one cross identifies the components, one gets different models, since there are uncertainties in it and multiple cross identifications are possible. The MOJAVE team identified three moving components (Lister et al. 2019). This model could be reproduced including two additional stationary components close to the core component. Furthermore a model with only stationary components was simulated. The results are shown in Sec.3. As it was pointed out in the Sec.4 there is no clear preference or arguments which would prefer one model over the other. As soon as the existing data will be calibrated and available one can compare these models. Deviations between the predicted and the observed jet structure might be indicative of accelerating or decelerating jet motions, which are predicted in structured-jet models to explain the apparent discrepancy between Doppler factors derived from radio and gamma-ray observations of high-peaked BL Lac objects (the so-called Doppler Crisis). So it means that since there are multiple possibilities of cross identifications one can not rely only on one model. As the next step one could apply a technique called Markov-Chain-Monte-Carlo (MCMC) in a Bayesian framework. This could help to identify the best number of components along with its uncertainties which gives even more information on the corresponding models. Eventually these simulations allow to limit

¹<https://www.cv.nrao.edu/MOJAVE/sourcepages/1514-241.shtml>

5. Conclusion and Outlook

the available possibilities to a smaller number.

A. Appendix

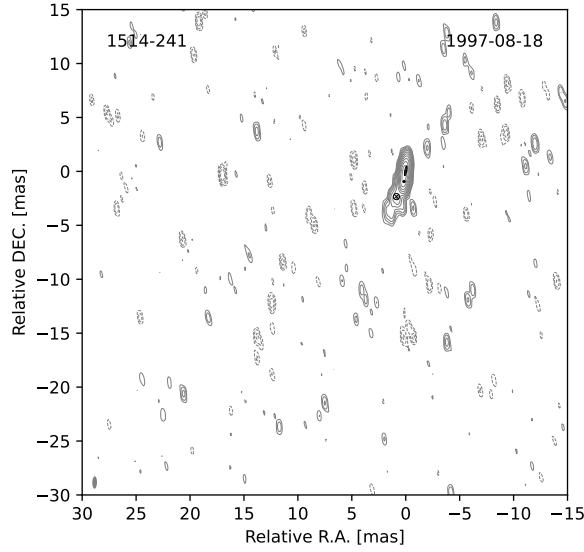


Figure A.1.: Naturally weighted clean image of 15 GHz MOJAVE observations of AP Librae in the 1997-08-18 epoch. The contours begin at 3σ and increase logarithmically by factors of 2. The gray ellipse in the bottom left corner corresponds to the beam. The fitted 2D Gaussian components are plotted overlaid

Date	Array	S_{tot}	S_{peak}	σ_{rms}	b_{maj}	b_{min}	P.A.
YYYY-MM-DD		[Jy]	[Jy/beam]	[mJy/beam]	[mas]	[mas]	[deg]
(1)	(2)	(3)	(4)	(5)	(6)	(7)	(8)
2020-07-11	PA-AT-MP-HO-CD- HH-WW-KE-YE	1.7	1.14	0.28	2.919	0.883	5.658

Table A.1.: Image parameters of the simulation. Col.(1): Date of observation. Col.(2): AT: ATCA, CD: Ceduna, HO: Hobart, MP: Mopra, PA: Parkes, KE: Katherine, HH: Hartebeesthoek, YE: Yarragadee, WW: Warkworth Col.(3): S_{tot} is the total flux density. Col.(4): S_{peak} is the peaked flux density of the core. Col.(5): σ_{rms} is the noise level. Col.(6): b_{maj} is the semi major axis of the beam. Col.(7): b_{min} is the semi minor axis of the beam. Col.(8): P.A.is the position angle of the beam.

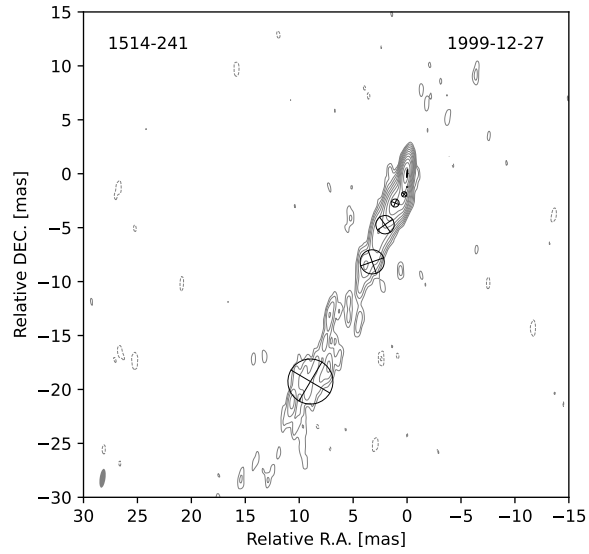


Figure A.2.: Naturally weighted clean image of 15 GHz MOJAVE observations of AP Librae in the 1999-12-27 epoch. The contours begin at 3σ and increase logarithmically by factors of 2. The gray ellipse in the bottom left corner corresponds to the beam. The fitted 2D Gaussian components are plotted overlaid

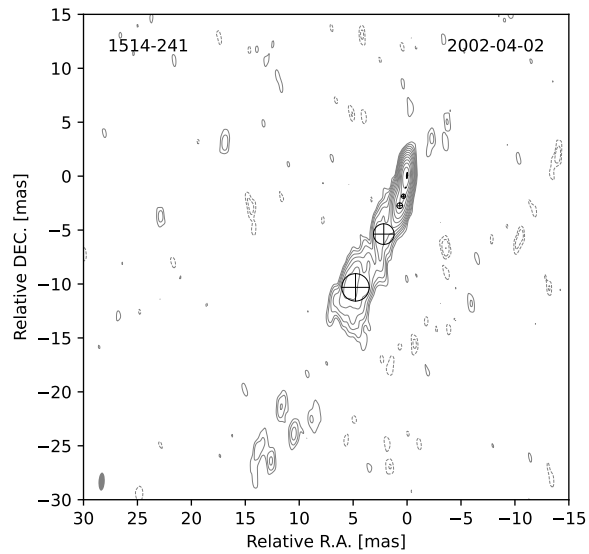


Figure A.3.: Naturally weighted clean image of 15 GHz MOJAVE observations of AP Librae in the 2002-04-02 epoch. The contours begin at 3σ and increase logarithmically by factors of 2. The gray ellipse in the bottom left corner corresponds to the beam. The fitted 2D Gaussian components are plotted overlaid

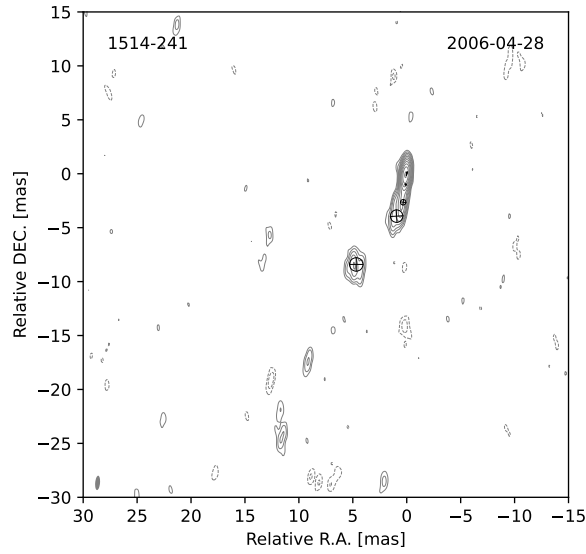


Figure A.4.: Naturally weighted clean image of 15 GHz MOJAVE observations of AP Librae in the 2006-04-28 epoch. The contours begin at 3σ and increase logarithmically by factors of 2. The gray ellipse in the bottom left corner corresponds to the beam. The fitted 2D Gaussian components are plotted overlaid

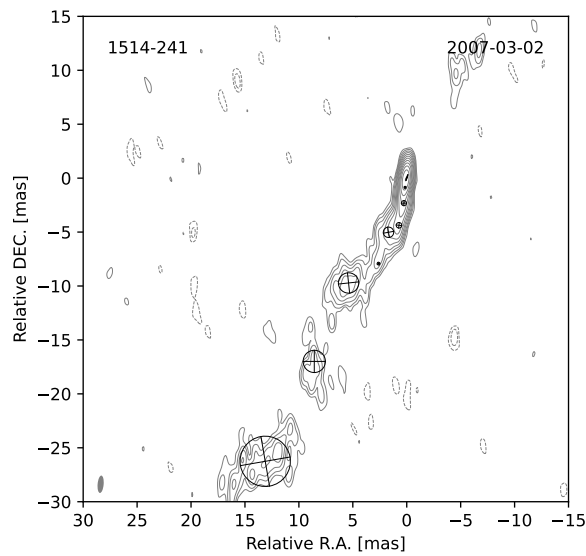


Figure A.5.: Naturally weighted clean image of 15 GHz MOJAVE observations of AP Librae in the 2007-03-02 epoch. The contours begin at 3σ and increase logarithmically by factors of 2. The gray ellipse in the bottom left corner corresponds to the beam. The fitted 2D Gaussian components are plotted overlaid

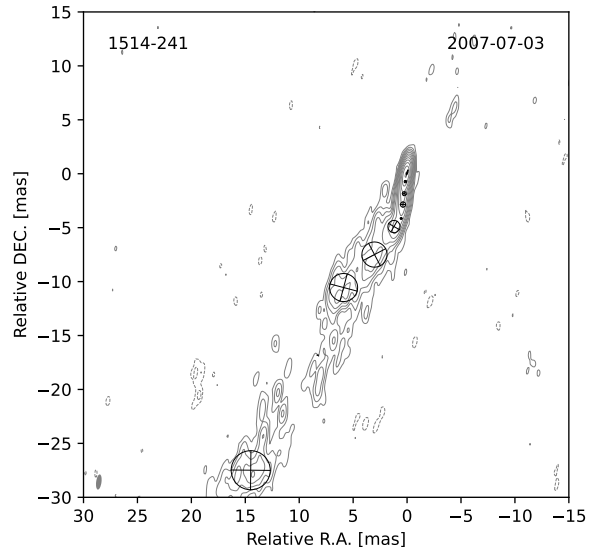


Figure A.6.: Naturally weighted clean image of 15 GHz MOJAVE observations of AP Librae in the 2007-07-03 epoch. The contours begin at 3σ and increase logarithmically by factors of 2. The gray ellipse in the bottom left corner corresponds to the beam. The fitted 2D Gaussian components are plotted overlaid

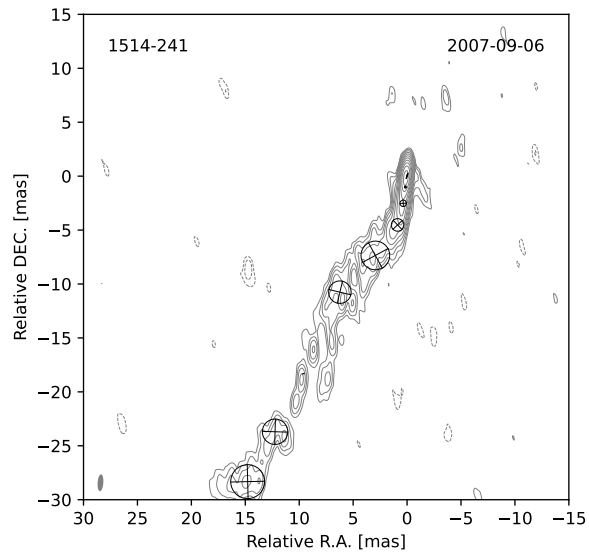


Figure A.7.: Naturally weighted clean image of 15 GHz MOJAVE observations of AP Librae in the 2007-09-06 epoch. The contours begin at 3σ and increase logarithmically by factors of 2. The gray ellipse in the bottom left corner corresponds to the beam. The fitted 2D Gaussian components are plotted overlaid

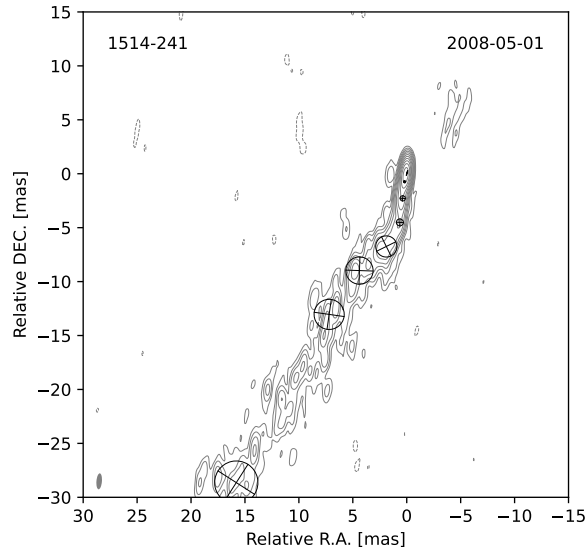


Figure A.8.: Naturally weighted clean image of 15 GHz MOJAVE observations of AP Librae in the 2008-05-01 epoch. The contours begin at 3σ and increase logarithmically by factors of 2. The gray ellipse in the bottom left corner corresponds to the beam. The fitted 2D Gaussian components are plotted overlaid

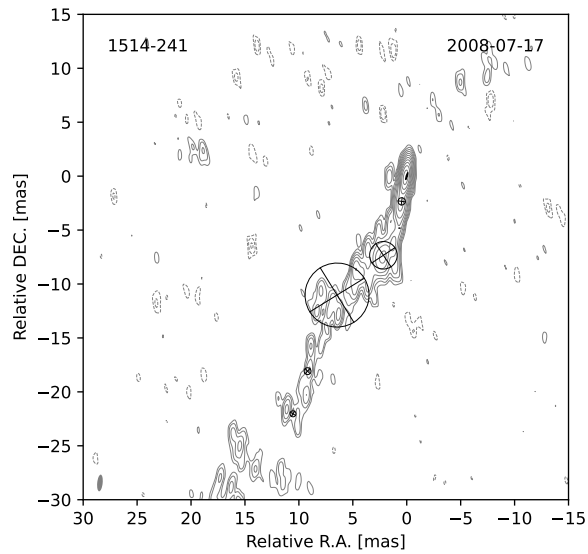


Figure A.9.: Naturally weighted clean image of 15 GHz MOJAVE observations of AP Librae in the 2008-07-17 epoch. The contours begin at 3σ and increase logarithmically by factors of 2. The gray ellipse in the bottom left corner corresponds to the beam. The fitted 2D Gaussian components are plotted overlaid

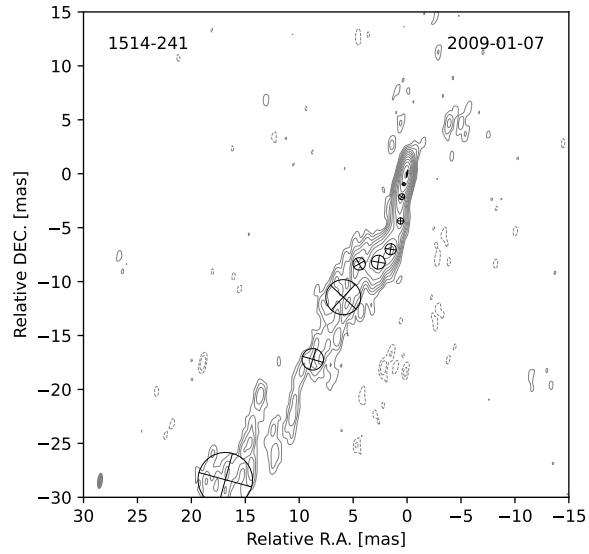


Figure A.10.: Naturally weighted clean image of 15 GHz MOJAVE observations of AP Librae in the 2009-01-07 epoch. The contours begin at 3σ and increase logarithmically by factors of 2. The gray ellipse in the bottom left corner corresponds to the beam. The fitted 2D Gaussian components are plotted overlaid

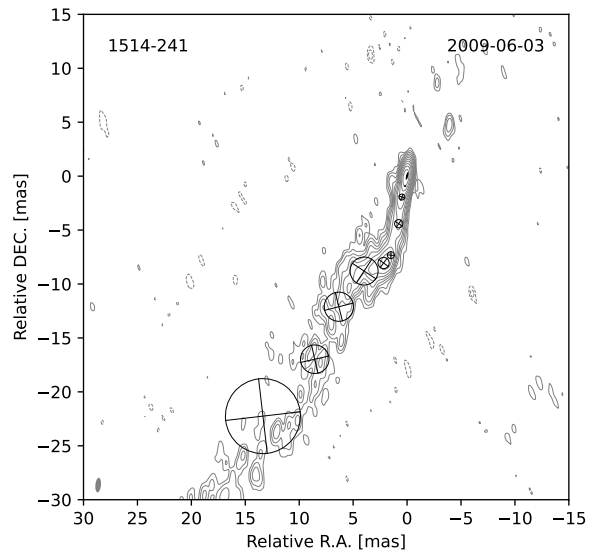


Figure A.11.: Naturally weighted clean image of 15 GHz MOJAVE observations of AP Librae in the 2009-06-03 epoch. The contours begin at 3σ and increase logarithmically by factors of 2. The gray ellipse in the bottom left corner corresponds to the beam. The fitted 2D Gaussian components are plotted overlaid

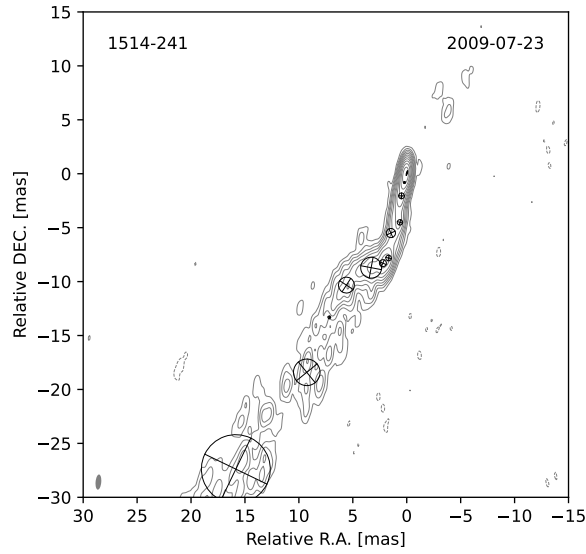


Figure A.12.: Naturally weighted clean image of 15 GHz MOJAVE observations of AP Librae in the 2009-07-23 epoch. The contours begin at 3σ and increase logarithmically by factors of 2. The gray ellipse in the bottom left corner corresponds to the beam. The fitted 2D Gaussian components are plotted overlaid

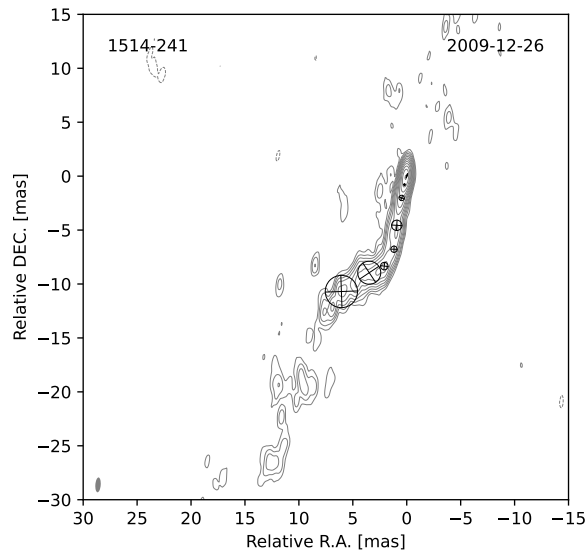


Figure A.13.: Naturally weighted clean image of 15 GHz MOJAVE observations of AP Librae in the 2009-12-26 epoch. The contours begin at 3σ and increase logarithmically by factors of 2. The gray ellipse in the bottom left corner corresponds to the beam. The fitted 2D Gaussian components are plotted overlaid

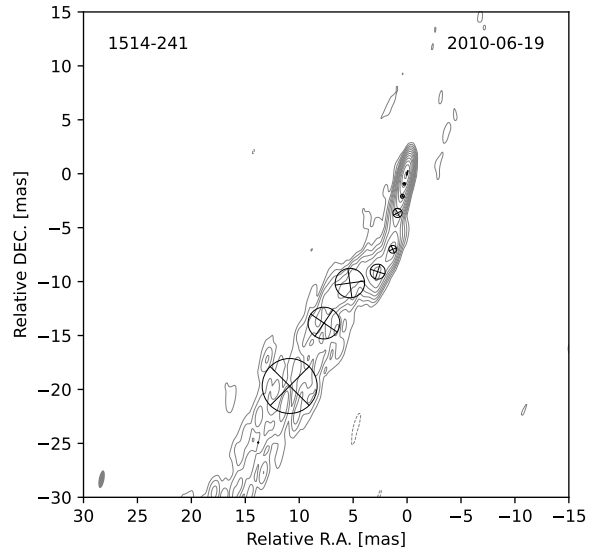


Figure A.14.: Naturally weighted clean image of 15 GHz MOJAVE observations of AP Librae in the 2010-06-19 epoch. The contours begin at 3σ and increase logarithmically by factors of 2. The gray ellipse in the bottom left corner corresponds to the beam. The fitted 2D Gaussian components are plotted overlaid

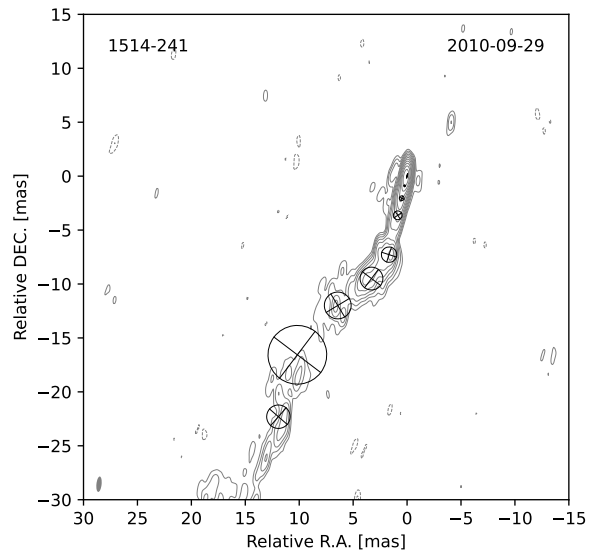


Figure A.15.: Naturally weighted clean image of 15 GHz MOJAVE observations of AP Librae in the 2010-09-29 epoch. The contours begin at 3σ and increase logarithmically by factors of 2. The gray ellipse in the bottom left corner corresponds to the beam. The fitted 2D Gaussian components are plotted overlaid

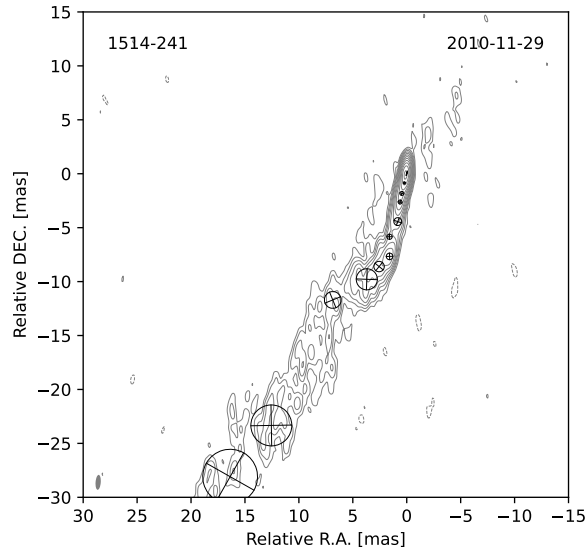


Figure A.16.: Naturally weighted clean image of 15 GHz MOJAVE observations of AP Librae in the 2010-11-29 epoch. The contours begin at 3σ and increase logarithmically by factors of 2. The gray ellipse in the bottom left corner corresponds to the beam. The fitted 2D Gaussian components are plotted overlaid

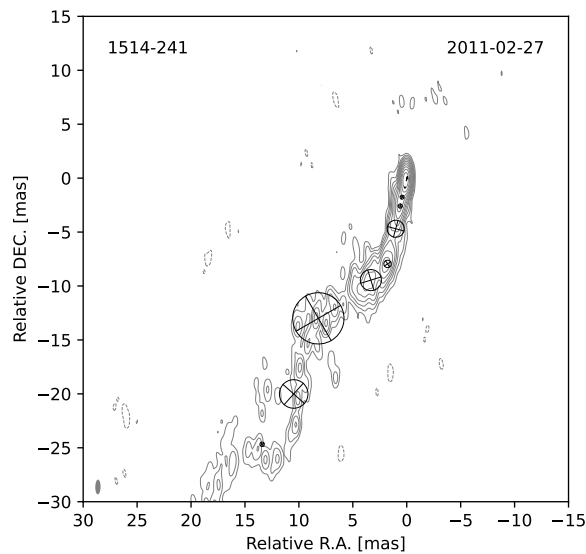


Figure A.17.: Naturally weighted clean image of 15 GHz MOJAVE observations of AP Librae in the 2011-02-27 epoch. The contours begin at 3σ and increase logarithmically by factors of 2. The gray ellipse in the bottom left corner corresponds to the beam. The fitted 2D Gaussian components are plotted overlaid

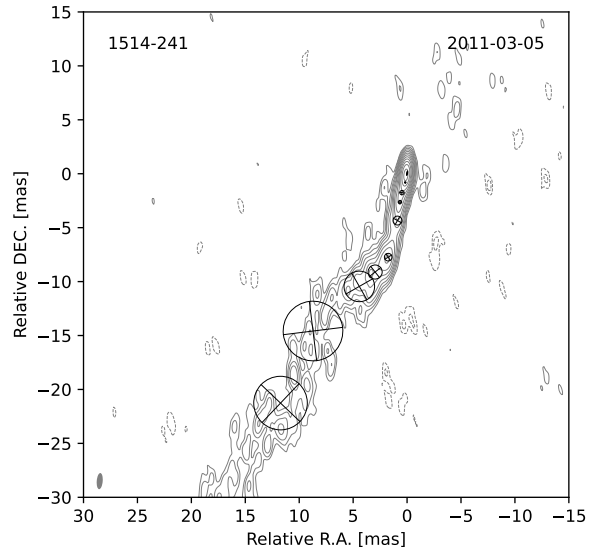


Figure A.18.: Naturally weighted clean image of 15 GHz MOJAVE observations of AP Librae in the 2011-03-05 epoch. The contours begin at 3σ and increase logarithmically by factors of 2. The gray ellipse in the bottom left corner corresponds to the beam. The fitted 2D Gaussian components are plotted overlaid

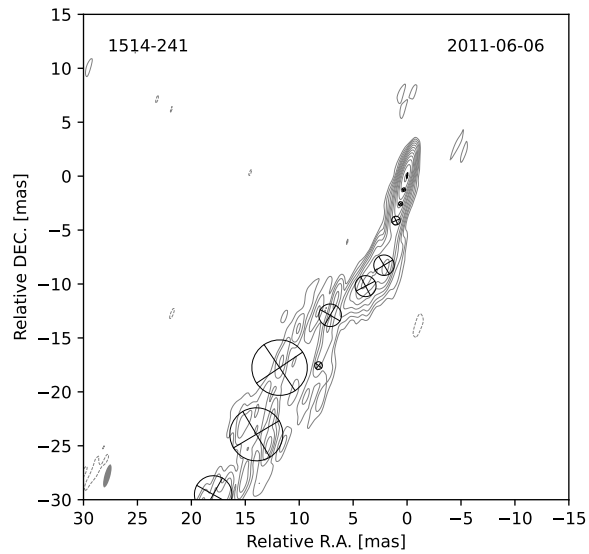


Figure A.19.: Naturally weighted clean image of 15 GHz MOJAVE observations of AP Librae in the 2011-06-06 epoch. The contours begin at 3σ and increase logarithmically by factors of 2. The gray ellipse in the bottom left corner corresponds to the beam. The fitted 2D Gaussian components are plotted overlaid

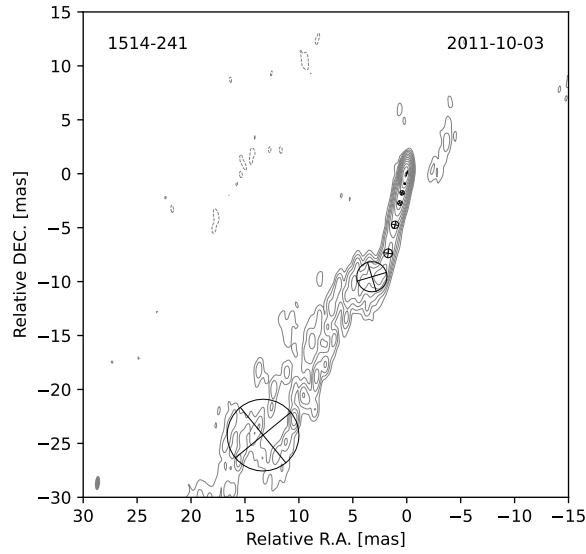


Figure A.20.: Naturally weighted clean image of 15 GHz MOJAVE observations of AP Librae in the 2011-10-03 epoch. The contours begin at 3σ and increase logarithmically by factors of 2. The gray ellipse in the bottom left corner corresponds to the beam. The fitted 2D Gaussian components are plotted overlaid

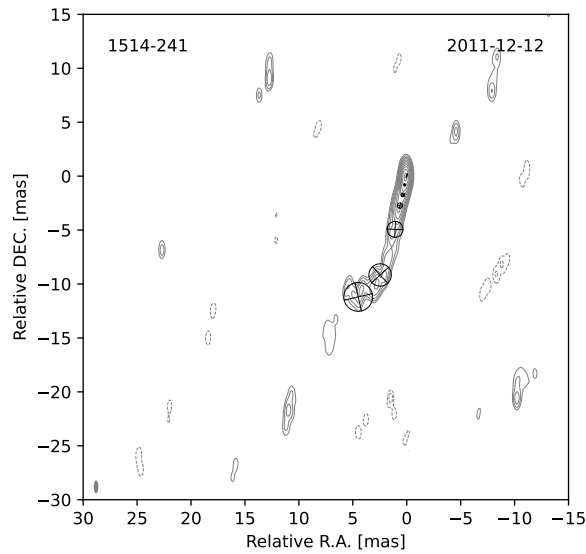


Figure A.21.: Naturally weighted clean image of 15 GHz MOJAVE observations of AP Librae in the 2011-12-12 epoch. The contours begin at 3σ and increase logarithmically by factors of 2. The gray ellipse in the bottom left corner corresponds to the beam. The fitted 2D Gaussian components are plotted overlaid

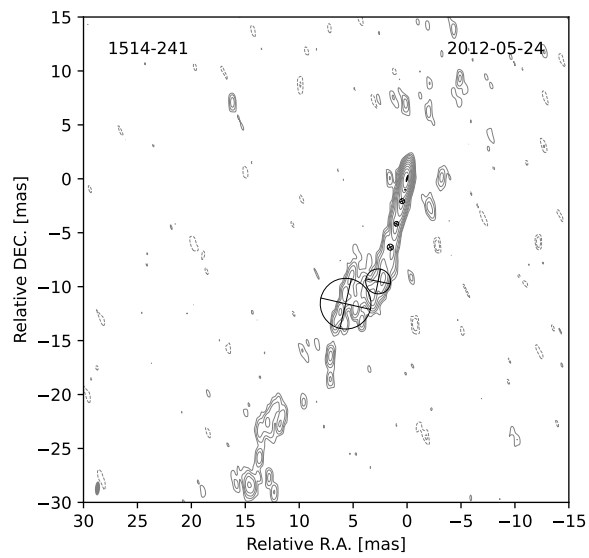


Figure A.22.: Naturally weighted clean image of 15 GHz MOJAVE observations of AP Librae in the 2012-05-24 epoch. The contours begin at 3σ and increase logarithmically by factors of 2. The gray ellipse in the bottom left corner corresponds to the beam. The fitted 2D Gaussian components are plotted overlaid

Date	Array	S_{tot}	S_{peak}	σ_{rms}	b_{maj}	b_{min}	P.A.
(1)	(2)	[Jy] (3)	[Jy/beam] (4)	[mJy/beam] (5)	[mas] (6)	[mas] (7)	[deg] (8)
1997-08-18	BR-FD-NH-KP-MK -NL-OV-PT-SC	2.12	1.2 0.23	1.157	0.436	-1.288	
1999-12-27	BR-FD-NH-KP-LA MK-NL-OV-PT-SC	2.13	1.14	0.26	1.766	0.536	-7.978
2002-04-02	BR-FD-NH-KP-LA MK-NL-OV-PT-SC	1.68	0.91	0.15	1.68	0.58	-3.23
2006-04-28	BR-FD-NH-KP-LA MK-NL-OV-PT-SC	2.27	1.75	0.51	1.337	0.446	-4.927
2007-03-02	BR-FD-NH-KP-LA MK-NL-OV-PT-SC	3.03	1.92	0.31	1.618	0.558	-4.985
2007-07-03	BR-FD-NH-KP-LA MK-NL-OV-PT-SC	2.59	1.39	0.21	1.419	0.493	-7.559
2007-09-06	BR-FD-KP-LA-MK- NL-OV-PT-SC	2.21	1.27	0.27	1.572	0.529	-3.958
2008-05-01	BR-FD-NH-KP-LA MK-OV-PT-SC	2.1	1.16	0.23	1.483	0.507	-4.606
2008-07-17	BR-FD-NH-KP-LA MK-NL-OV-PT-SC	2.0	1.15	0.24	1.553	0.504	-5.808
2009-01-07	BR-FD-NH-KP-LA MK-NL-OV-PT-SC	2.04	1.03	0.16	1.529	0.54	-6.788
2009-06-03	BR-FD-NH-KP-LA MK-NL-OV-PT-SC	2.26	1.06	0.18	1.358	0.515	-5.577
2009-07-23	BR-FD-NH-KP-LA MK-NL-OV-PT-SC	2.25	1.11	0.2	1.412	0.525	-4.953
2009-12-26	BR-FD-NH-KP-LA MK-NL-OV-PT-SC	1.83	1.04	0.16	1.377	0.496	-4.218
2010-06-19	BR-FD-NH-KP-LA MK-NL-OV-PT-SC	2.04	1.17	0.17	1.675	0.527	-10.682
2010-09-29	BR-FD-NH-KP-LA MK-OV-PT-SC	2.03	1.2	0.2	1.437	0.479	-5.952
2010-11-29	BR-FD-NH-KP-LA MK-NL-OV-PT-SC	1.99	1.17	0.15	1.389	0.479	-4.303
2011-02-27	BR-FD-NH-KP-LA MK-NL-OV-PT-SC	2.07	1.23	0.21	1.367	0.489	-0.842
2011-03-05	BR-FD-NH-KP-LA MK-NL-OV-PT-SC	2.17	1.34	0.16	1.502	0.552	-4.599
2011-06-06	BR-FD-NH-KP-LA MK-NL-OV-PT-SC	2.08	1.34	0.2	2.208	0.544	-15.38
2011-10-03	BR-FD-NH-KP-LA MK-NL-OV-PT-SC	2.09	1.25	0.19	1.327	0.474	-4.931
2011-12-12	BR-FD-NH-KP-LA MK-NL-OV-PT-SC	1.85	1.16	0.3	1.197	0.434	-0.229
2012-05-24	BR-FD-KP-LA-MK- NL-OV-PT-SC	2.1	1.26	0.2	1.297	0.469	-4.392

Table A.2.: Image and observation parameters (mojave team). Col(1): Date of observation. Col(2): BR: Brewster – Washington, FD: Fort Davis – Texas, NH: Hancock – New Hampshire, KP: Kitt Peak – Arizona, LA: Los Alamos – New Mexico, MK: Mauna Kea – Hawaii, NL:North Liberty – Iowa, OV: Owens Valley – California, PT: Pie Town – New Mexico, SC: St. Croix – U.S. Virgin Islands. Col.(3): S_{tot} is the total flux density. Col.(4): S_{peak} is the peaked flux density of the core. Col.(5): σ_{rms} is the noise level. Col.(6): b_{maj} is the semi major axis of the beam. Col.(7): b_{min} is the semi minor axis of the beam. Col.(8): P.A.is the position angle of the beam.

A. Appendix

Flux density [Jy]	Major Axis [mas]	Ratio	PA [deg]	Dist [mas]	Comp ID Nr
1997-08-18					
1.649	0.903	0.206	-11.468	0.000	Core
0.441	0.187	1.000	-81.870	1.008	C2
0.102	0.575	1.000	-137.603	2.542	C4
1999-12-27					
0.023	0.214	1.000	-82.875	1.247	0*
1.203	0.717	0.046	-3.936	0.000	C1*
0.394	0.489	1.000	-40.815	1.945	C3
0.322	0.741	1.000	-22.479	2.949	C4
0.140	1.702	1.000	-54.462	5.162	C5
0.082	2.238	1.000	-160.641	8.801	C6
0.013	4.178	1.000	-30.579	21.263	C8
2002-04-02					
0.954	0.546	0.201	-4.723	0.000	Core
0.090	0.062	1.000	-26.003	1.133	C2*
0.207	0.393	1.000	-82.235	1.956	C3
0.209	0.531	1.000	-85.236	2.888	C4
0.071	1.913	1.000	-90.000	5.854	C5
0.171	2.544	1.000	-90.000	11.426	C7
2006-04-28					
1.805	0.334	0.141	-13.777	0.000	Core
0.149	0.125	1.000	-32.905	1.020	C2
0.188	0.507	1.000	-7.352	2.678	C3
0.118	1.159	1.000	-86.634	4.058	C4
0.101	1.250	1.000	-90.000	9.639	C7
2007-03-02					
0.151	0.516	1.000	-96.483	4.487	0
1.920	0.548	0.099	-18.160	0.000	Core
0.359	0.187	1.000	-45.000	0.923	C2
0.282	0.476	1.000	-90.000	2.388	C3
0.075	0.966	1.000	-79.992	5.355	C5
0.022	0.306	1.000	-157.906	8.404	C6*
0.116	1.883	1.000	-83.884	11.171	C7
0.034	2.064	1.000	-90.000	19.089	C8
0.122	4.663	1.000	-80.134	29.407	C9
2007-07-03					
0.041	0.181	1.000	-15.642	4.303	0
0.182	0.485	1.000	-90.000	3.004	0
1.291	0.454	0.173	-16.682	0.000	Core
0.503	0.221	1.000	-45.000	0.870	C2
0.166	0.368	1.000	-21.318	1.992	C3
0.128	1.134	1.000	-29.899	5.167	C5
0.102	2.336	1.000	-62.354	8.200	C6
0.103	2.602	1.000	165.174	12.197	C7
0.009	0.198	1.000	-21.501	18.892	C8*
0.097	3.623	1.000	-0.591	31.192	C9
2007-09-06					
1.305	0.505	0.121	-17.368	0.000	Core
0.238	0.178	1.000	-15.350	1.047	C2
0.262	0.603	1.000	-87.510	2.570	C3
0.138	1.167	1.000	-46.302	4.635	C5
0.110	2.660	1.000	-61.526	7.943	C6
0.072	2.084	1.000	-103.610	12.454	C7
0.016	0.435	1.000	-90.000	20.724	C8*
0.043	2.355	1.000	-91.736	26.696	C9
0.075	3.146	1.000	-88.636	31.971	C10
2008-05-01					
0.052	2.795	1.000	171.849	14.966	0
1.131	0.438	0.093	-15.437	0.000	Core
0.262	0.202	1.000	19.314	0.840	C2
0.245	0.491	1.000	-3.904	2.385	C3
0.097	0.649	1.000	-93.305	4.630	C4
0.199	1.964	1.000	26.326	7.077	C5
0.088	2.529	1.000	-1.954	10.063	C7

Flux density [Jy]	Major Axis [mas]	Ratio	PA [deg]	Dist [mas]	Comp ID Nr
2008-07-17					
0.034	0.639	1.000	-44.700	20.283	0
1.322	0.649	0.160	-16.146	0.000	Core
0.244	0.674	1.000	-7.516	2.384	C3
0.033	0.197	1.000	-15.788	4.872	C4*
0.266	2.552	1.000	-146.586	7.650	C5
0.159	5.933	1.000	-58.303	12.778	C7
0.023	0.613	1.000	-122.547	24.427	C8*
2009-01-07					
0.015	1.993	1.000	163.465	19.318	0
0.061	3.244	1.000	-43.152	12.896	0
1.102	0.634	0.175	-9.299	0.000	Core
0.172	0.290	1.000	7.685	1.022	C2
0.201	0.545	1.000	-29.487	2.202	C3
0.088	0.584	1.000	-1.771	4.432	C4
0.169	1.024	1.000	-8.162	7.179	C5
0.177	1.281	1.000	-9.607	8.634	C6
0.061	1.154	1.000	-150.305	9.481	C7
0.040	5.056	1.000	-15.243	33.013	C10
2009-06-03					
0.031	2.646	1.000	-77.146	19.027	0
0.059	2.706	1.000	-75.822	13.678	0
1.151	0.558	0.165	-14.019	0.000	Core
0.130	0.023	1.000	-154.232	0.976	C2*
0.226	0.554	1.000	-21.901	2.013	C3
0.112	0.769	1.000	-33.414	4.496	C4
0.134	0.649	1.000	-3.653	7.498	C5
0.209	1.044	1.000	-36.183	8.361	C6
0.206	2.598	1.000	-33.414	9.676	C7
0.045	6.954	1.000	-83.349	25.972	C9
2009-07-23					
0.012	0.304	1.000	-20.360	15.183	0*
0.193	1.940	1.000	169.270	9.374	0
0.114	0.519	1.000	-10.929	8.054	0
0.097	0.504	1.000	-16.535	4.609	0
1.109	0.439	0.198	-14.622	0.000	Core
0.245	0.175	1.000	-32.811	0.894	C2
0.217	0.540	1.000	-1.157	2.168	C3
0.059	0.865	1.000	-65.814	5.752	C4*
0.093	0.648	1.000	-23.280	8.641	C6
0.068	1.473	1.000	-33.000	11.801	C7
0.019	2.463	1.000	-50.877	20.672	C8
0.076	6.387	1.000	-25.707	31.697	C10
2009-12-26					
0.138	2.136	1.000	-146.301	9.647	0
0.055	0.586	1.000	-1.050	6.921	0
1.017	0.369	0.100	-16.015	0.000	Core
0.249	0.156	1.000	-10.453	0.858	C2
0.159	0.500	1.000	-20.227	2.117	C3
0.095	0.960	1.000	-3.477	4.696	C4
0.069	0.698	1.000	-6.495	8.638	C6
0.080	2.991	1.000	-177.976	12.336	C7
2010-06-19					
0.026	7.090	1.000	154.329	49.187	0
0.054	2.944	1.000	-124.255	15.926	0
0.095	0.721	1.000	22.459	7.213	0
1.116	0.433	0.155	-15.007	0.000	Core
0.295	0.243	1.000	-19.104	1.054	C2
0.145	0.360	1.000	161.440	2.217	C3
0.069	0.851	1.000	28.359	3.824	C4
0.144	1.395	1.000	161.945	9.563	C6
0.088	2.732	1.000	7.898	11.520	C7
0.049	5.094	1.000	-134.882	22.569	C8
0.007	0.288	1.000	-9.366	28.568	C9*

A. Appendix

Flux density [Jy]	Major Axis [mas]	Ratio	PA [deg]	Dist [mas]	Comp ID Nr
2010-09-29					
0.030	2.174	1.000	-131.112	25.320	0
1.218	0.412	0.150	-13.142	0.000	Core
0.188	0.153	1.000	-95.249	0.956	C2
0.212	0.437	1.000	-21.410	2.131	C3
0.053	0.814	1.000	-146.119	3.759	C4
0.176	1.422	1.000	-108.016	7.495	C5
0.135	2.116	1.000	-36.978	10.079	C6
0.043	2.486	1.000	31.027	13.630	C7
0.055	5.441	1.000	52.842	19.464	C8
2010-11-29					
0.021	1.555	1.000	22.130	13.597	0
0.017	0.486	1.000	0.756	6.093	0
0.095	0.365	1.000	-8.508	2.732	0
1.187	0.406	0.126	-15.653	0.000	Core
0.185	0.200	1.000	18.560	0.915	C2
0.138	0.371	1.000	-16.733	1.915	C3
0.043	0.728	1.000	-19.465	4.551	C4
0.104	0.610	1.000	2.024	7.865	C5
0.064	0.967	1.000	51.047	9.016	C6
0.085	1.954	1.000	-2.139	10.501	C7
0.052	3.795	1.000	0.977	26.532	C9
0.049	5.078	1.000	-119.525	32.545	C10
2011-02-27					
0.013	0.584	1.000	-146.586	35.295	0
0.065	4.760	1.000	-59.996	15.331	0
0.071	1.584	1.000	-15.224	4.757	0
1.253	0.389	0.026	-13.789	0.000	Core*
0.156	0.069	1.000	15.003	0.841	C2
0.113	0.362	1.000	-23.552	1.773	C3
0.114	0.383	1.000	-7.052	2.613	C4
0.121	0.688	1.000	33.414	8.104	C6
0.161	1.954	1.000	-72.811	9.981	C7
0.025	2.648	1.000	138.234	22.552	C8
0.012	0.408	1.000	123.968	28.049	C9
2011-03-05					
0.098	1.307	1.000	38.273	9.629	0
0.060	0.827	1.000	-29.487	4.481	0
1.334	0.387	0.200	-10.092	0.000	Core
0.164	0.122	1.000	15.686	0.877	C2
0.147	0.401	1.000	-6.965	1.864	C3
0.086	0.310	1.000	-177.927	2.759	C4
0.129	0.706	1.000	31.837	7.980	C6
0.081	2.834	1.000	29.673	11.394	C7
0.074	5.531	1.000	7.052	17.037	C8
0.058	4.968	1.000	-43.577	24.332	C9
2011-06-06					
0.015	3.488	1.000	-29.102	34.614	0
0.012	0.716	1.000	-128.097	19.444	0
0.029	2.095	1.000	-119.734	14.795	0
0.058	0.806	1.000	-155.781	4.302	0
0.216	0.321	1.000	-16.935	1.346	0
1.319	0.513	0.179	-9.189	0.000	Core
0.123	0.386	1.000	-145.289	2.687	C3
0.169	1.899	1.000	-149.047	8.587	C6
0.114	1.950	1.000	-152.423	10.956	C7
0.023	5.145	1.000	-146.030	21.384	C9
0.049	4.920	1.000	-149.300	27.772	C10

Flux density [Jy]	Major Axis [mas]	Ratio	PA [deg]	Dist [mas]	Comp ID Nr
2011-10-03					
0.057	0.679	1.000	167.888	4.890	0
0.134	0.420	1.000	-162.182	2.822	0
1.306	0.458	0.114	-15.730	0.000	Core
0.164	0.151	1.000	-163.702	0.979	C2
0.121	0.409	1.000	-23.585	1.858	C3
0.045	0.811	1.000	171.660	7.608	C6
0.192	2.790	1.000	-163.465	10.117	C7
0.128	6.644	1.000	-140.576	27.684	C10
2011-12-12					
0.136	2.077	1.000	-137.589	9.539	0
1.192	0.352	0.183	-17.508	0.000	Core
0.295	0.181	1.000	22.481	0.870	C2
0.104	0.346	1.000	-148.145	1.821	C3
0.127	0.492	1.000	-14.869	2.855	C4
0.091	1.472	1.000	177.536	5.100	C5
0.101	2.670	1.000	-167.184	12.115	C7
2012-05-24					
0.147	4.704	1.000	167.040	12.926	0
1.412	0.545	0.175	-13.916	0.000	Core
0.151	0.067	1.000	-26.326	1.065	C2*
0.168	0.457	1.000	20.031	2.144	C3
0.067	0.437	1.000	155.781	4.309	C4
0.044	0.565	1.000	-148.534	6.549	C6
0.161	2.308	1.000	168.582	9.903	C7

Table A.3.: Simulation parameters of each component with flux density, major and minor axis of the components, the ratio of the major to minor axis, P.A is the position angle of the components, Dist is the distance from the core and the ID number of the corresponding component. Components marked with a star symbolize that either the major or minor axis was not resolved and was replaced with corresponding resolution limit.

Bibliography

- Asada K., Nakamura M., 2012, *The Astrophysical Journal Letters*, 745, L28
- Burd P., et al., 2022, *Astronomy & Astrophysics*, 660, A1
- Burke B. F., Graham-Smith F., Wilkinson P. N., 2019, *An introduction to radio astronomy*. Cambridge University Press
- Burtscher L., et al., 2013, *Astronomy & Astrophysics*, 558, 46
- Carroll B. W., Ostlie D. A., 2017, *An introduction to modern astrophysics*. Cambridge University Press
- Cerruti M., Zech A., Emery G., Guarin D., 2017, in *AIP Conference Proceedings*.
- Fanaroff B. L., Riley J. M., 1974, *Monthly Notices of the Royal Astronomical Society*, 167, 31
- Hervet O., Boisson C., Sol H., 2015, *Astronomy & Astrophysics*, 578, 11
- Högbom J., 1974, *Astronomy and Astrophysics Supplement*, 15, 417
- Kadler M., Ros E., Lobanov A., Falcke H., Zensus J., 2004, *Astronomy & Astrophysics*, 426, 481
- Kadler M., Ojha R., Collaboration T., et al., 2015, *Astronomische Nachrichten*, 336, 499
- Kadler M., et al., 2016, *Nature Physics*, 12, 807
- Kellermann K., Sramek R., Schmidt M., Shaffer D., Green R., 1989, *The Astronomical Journal*, 98, 1195
- Kembhavi A. K., Narlikar J. V., 1999, *Quasars and active galactic nuclei: an introduction*. Cambridge University Press
- Kovalev Y. Y., et al., 2005, *The Astronomical Journal*, 130, 2473
- Lister M., et al., 2019, *The Astrophysical Journal*, 874, 43
- Longair M., 2011, *High Energy Astrophysics 3rd edition*. Cambridge University Press

BIBLIOGRAPHY

- Mannheim K., 1993, *Astronomy and Astrophysics*, 269, 67
- Mannheim K., Biermann P., 1992, *Astronomy and Astrophysics*, 253, L21
- Müller C., 2014, PhD thesis, Friedrich-Alexander-Universität Erlangen-Nürnberg (FAU)
- Padovani P., 1999, *Vulcano Workshop 1998: Frontier Objects in Astrophysics and Particle Physics*, 65, 159
- Padovani P., et al., 2017, *The Astronomy and Astrophysics Review*, 25, 1
- Rees M., 1966, *Nature*, 211, 468
- Rösch F., et al., 2022, in *European VLBI Network Mini-Symposium and Users' Meeting 2021*.
- Rybicki G., Lightman A., 1979, *Radiative Processes in Astrophysics*, A Wiley, New York
- Shields G. A., 1999, *Publications of the Astronomical Society of the Pacific*, 111, 661
- Taylor G., 1994, *The Difmap Cookbook*. California Institute of Technology Pasadena
- Urry C. M., Padovani P., 1995, *Publications of the Astronomical Society of the Pacific*, 107, 803
- Wang F., et al., 2021, *The Astrophysical Journal Letters*, 907, 7

Dankesagung

An dieser Stelle würde ich gerne an alle meinen Dank aussprechen, die zum Gelingen dieser Arbeit beigetragen haben. Zuallererst bedanke ich mich bei Prof. Dr. Matthias Kadler, der mir dieses interessante Projekt ermöglicht hat. Durch die gesamte Arbeit hindurch setzte Matthias wichtige Impulse, um das Projekt in die richtige Richtung zu lenken. Zudem wurde mir die Ehre zuteil, Teilergebnisse dieser Arbeit bei der IBWS Konferenz in Karlsbad vorstellen zu dürfen, wofür ich ebenfalls sehr dankbar bin.

Besonderer Dank gebührt meinem Betreuer Florian Rösch, der mir seit dem astrophysikalischen Praktikum und durch die gesamte Arbeit hindurch stets sehr hilfsbereit mit Rat und Tat zur Seite stand. Seine Ideen und Ratschläge sowie die höchst sorgfältige und professionelle Herangehensweise samt unzähligen Stunden an Arbeit haben mir und dieser Arbeit sehr geholfen. Vielen Dank auch für das akribische Korrekturlesen, welches mein Verständnis und das Niveau der Arbeit deutlich gesteigert hat.

Ebenfalls einen sehr großen Anteil am Erfolg dieser Arbeit hatte Dr. Christian Fromm, der die Software zur Simulation bereitgestellt hat und dem ich an dieser Stelle danken will.

Außerdem möchte ich allen Mitarbeitern der Lehrstuhls für Astronomie unter der Leitung von Prof. Dr. Karl Mannheim, vor allem aber den Mitgliedern der AG Kadler, für die herzliche Aufnahme, Einarbeitung und Unterstützung danken. Insbesondere den Kollegen Philip Weber, Jonas Heßdörfer sowie Felix Pfeifle, die mich in ihrem Büro samt der sehr angenehmen Arbeitsatmosphäre aufgenommen haben und stets für Fragen und Diskussionen offenstanden, möchte ich danken. Vielen Dank zusätzlich an Jonas für das Korrekturlesen meiner Arbeit.

Zum Schluss möchte ich noch meinem privaten Umfeld danken, welches mich zu dem Menschen gemacht hat, der ich heute bin. Danke an alle Freunde, Bekannte und Verwandte, die Teil meiner Reise waren und ebenso ihren Teil zum Erfolg beigetragen haben. Der allerletzte Dank gehört meinen Eltern, meinen Geschwistern und meiner Freundin. Vielen Dank für die Unterstützung.

Selbstständigkeitserklärung

Hiermit erkläre ich, dass ich die vorliegende Arbeit mit dem Titel *Long-Term Jet-Kinematics of Blazars in the TANAMI Sample* selbstständig verfasst und keine anderen als die angegebenen Quellen und Hilfsmittel verwendet habe. Die Arbeit wurde in gleicher oder ähnlicher Form keiner anderen Prüfungsbehörde vorgelegt und auch nicht veröffentlicht.

Würzburg, den 28.07.2023

A handwritten signature in black ink, reading "Schreyer. W.", written over a horizontal line.

Unterschrift